Nucleic Acids Research, 2025, **53**, gkaf650
https://doi.org/10.1093/nar/gkaf650
Gene regulation, Chromatin and Epigenetics

BAHCC1 promotes gene expression in neuronal cells by antagonizing SIN3A–HDAC1

Alan Monziani, Rotem Ben-Tov Perry, Hadas Hezroni, Igor Ulitsky *

Department of Immunology and Regenerative Biology and Department of Molecular Neuroscience, Weizmann Institute of Science, Rehovot, 76100, Israel

*To whom correspondence should be addressed. Email: igor.ulitsky@weizmann.ac.il

Abstract

Chromatin modifications play a key role in regulating gene expression during development and adult physiology. Histone acetylation, particularly H3K27ac, is associated with increased activity of gene regulatory elements such as enhancers and promoters. However, the regulation of the machinery that writes, reads, and erases this modification remains poorly understood. In particular, the SIN3A–HDAC1 complex possesses histone deacetylase activity, yet it commonly resides at active regulatory regions. Here, we study BAHCC1, a large chromatin-associated protein essential for viability and recently reported to play a largely repressive role. We show that in neuronal lineage cells, BAHCC1 is mainly associated with regulatory elements marked with H3K27ac. BAHCC1 interacts and co-occupies shared genomic regions with the SIN3A scaffold protein, but not with its paralog SIN3B, and its perturbations lead to altered acetylation and expression of proximal genes in a neuronal cell line and primary cortical neurons. The regulated genes are enriched for those functioning in neurogenesis and cell migration, and primary cortical neurons with reduced *Bahcc1* expression display impaired neurite outgrowth. We thus propose a model in which BAHCC1 antagonizes SIN3A histone deacetylation and positively regulates the expression of genes that are important for growth and migration-related processes in the neuronal lineage.

Graphical abstract

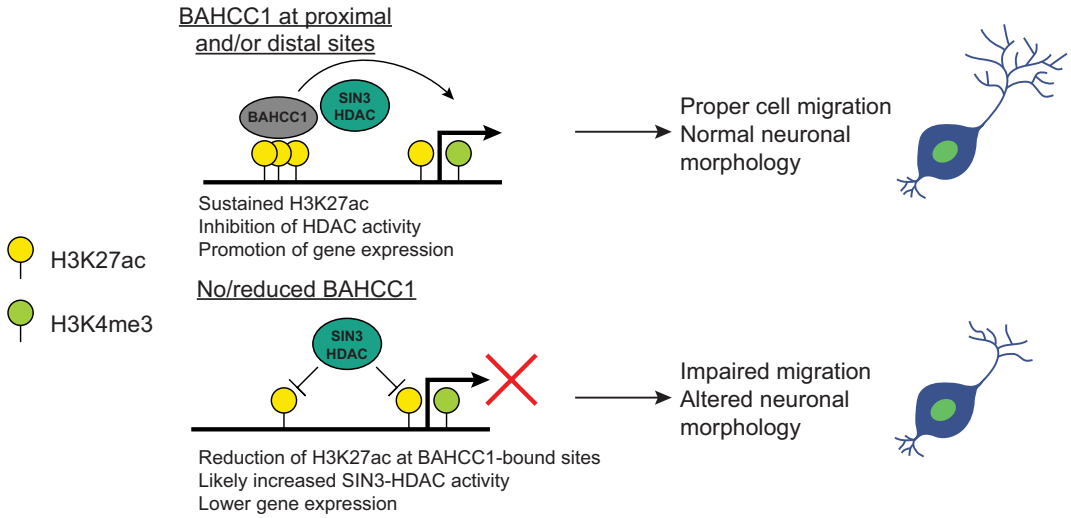

Introduction

Regulation of gene expression plays a central role in establishing cell type identity during embryonic development and the response of cells to external stimuli throughout their lifetime. Gene expression is regulated by combinations of regulatory elements found at promoters and enhancers, whose accessibility and activity are modulated by chromatin conformation and histone marks. Various proteins and protein complexes write, read, and erase the histone marks [1]. While the activity of some of these complexes, such as the repressive Polycomb PRC1 and PRC2 complexes, has been extensively studied and is reasonably well understood, others remain largely obscure [2, 3]. SIN3A and the related SIN3B proteins are at the heart of the Sin3 multisubunit complexes. The structure of the SIN3A complex has been resolved, and it contains 13 core proteins, with SIN3A acting as the main protein scaffold [4]. Loss of

Received: December 12, 2024. **Revised:** June 12, 2025. **Editorial Decision:** June 13, 2025. **Accepted:** June 20, 2025

function of the core members of Sin3 results in early embryonic lethality [5–8], suggesting a crucial role during early development, yet its biological function remains largely unclear. The Sin3 complex contains HDAC1, a histone deacetylase associated with gene repression. Sin3 was traditionally thought to have repressive roles [9, 10], as recruitment of SIN3A is sufficient for inducing repression at target promoters [11, 12]. However, HDAC1 is also part of the NuRD and CoREST complexes, and other HDACs also deacetylate histones, so the relative contribution of SIN3A is unclear. Chromatin profiling studies located Sin3a complexes at active promoters in mouse embryonic stem cells (mESCs) [13] and other systems [14, 15], casting doubt on whether it regulates gene expression negatively or positively.

BAHCC1 is a poorly studied chromatin-associated protein. BAHCC1 is a ∼280 kD protein conserved throughout vertebrates and characterized by a BAH domain found at its C-terminus and a pair of Tudor domains. Its expression is upregulated in acute lymphoblastic leukemia (ALL) of T-cell or B-cell lineages (T-ALL or B-ALL) and in melanoma, and its depletion affects the proliferation of leukemic and melanoma cells [16, 17]. BAHCC1 is an ortholog of the D. melanogaster *winged eye* (wge) and a paralog of TNRC18, both of which were implicated in different gene expression regulation steps [18–20]. A recent study has shown that the BAH domain of BAHCC1 binds the H3K27me3 repressive mark and suggested that BAHCC1 acts as a "reader" of H3K27me3 marks and represses gene expression in blood cells [16], though most of the biochemical characterization focused on just the C-terminal BAH domain, which accounts for just ∼5% of the full protein. In contrast, BAHCC1 was predominantly associated with active H3K27ac-demarcated regions and positively regulated gene expression in melanoma cells [17].

We recently studied *Bahcc1* in mESCs and early neuronal progenitors in a study focused on a neighboring gene, a long noncoding RNA called *Reno1* [21]. We found that KO of *Bahcc1* or *Reno1* inhibited neuronal differentiation of mESCs and triggered cell death, consistent with a defect in neurogenesis upon knockdown (KD) of BAHCC1 in another study [22]. We also found that KO of BAHCC1 led to a substantial reduction of chromatin accessibility at regions marked by H3K4me3 and the SIN3A–FAM60A complex in mESCs [21]. Other studies have shown that BAHCC1 co-immunoprecipitates with members of the SIN3A complex, including HDAC1, SAP30, FAM60A, RBBP4, RBBP7, and ING2 [13, 16, 23–26]. Additional data point to the importance of BAHCC1 in the neuronal lineage—*Bahcc1* messenger RNA (mRNA) is preferentially expressed in the developing brain over other tissues [21], and *Bahcc1*$^{-/-}$ mice exhibit perinatal lethality, with one mouse reported to show defective motor neuron development [27]. The requirement of BAHCC1 for embryonic development and postnatal survival was also observed in another mouse model carrying a specific mutation in the BAH domain [16]. In this study, we focused on the gene regulatory roles of BAHCC1 in neuronal lineage cells.

Materials and methods

Cell culture and transfection

Neuro2a (N2a) and HEK293T cells were cultured in Dulbecco's Modified Eagle Medium (DMEM) supplemented with 4.5 g/l of glucose, 4 mM L-glutamine, 10% Fetal Bovine Serum (FBS), 1% PenStrep solution; grown in incubators maintained at 37°C with 5% CO_2; and were routinely passaged by gentle dissociation using a trypsin (0.05%)–ethylenediaminetetraacetic acid (EDTA) (0.02%) solution. DNA plasmid transfections were performed by using Lipofectamine 3000 (Thermo Fisher Scientific), according to the respective protocols. For each transfection, the optimal DNA concentration and amount of transfection reagents were empirically determined to minimize cellular stress and maximize efficiency, to eventually ensure clean readouts. To induce the expression of doxycycline-inducible plasmids, cells were cultured in the presence of doxycycline at a final concentration of 2 μg/μl. Small Interfering RNAs (siRNAs) were transfected using DharmaFECT reagents (DharmaFECT 2), at a final concentration of 25 μM concordantly to the manufacturer's protocol. GapmeRs were transfected at the final concentration of 50 μM with Lipofectamine 3000, following the manufacturer's guidelines. In all cases, cells were plated the day before the transfection in an antibiotic-free medium, which was subsequently changed prior to adding the transfection mix and again after 24 h to minimize cell death. Finally, transfections were carried out for 72 h, unless stated otherwise. The complete list with the catalog numbers and sequences of both siRNAs and LNA/GapmeRs is reported in Supplementary Table S1.

Primary neuronal culture and morphological analysis

All of the animals were handled according to approved institutional animal care and use committee protocols of the Weizmann Institute of Science (permit number 03580421-3). Every effort was made to minimize suffering. Embryonic cortices (embryonic day 16.5–17) were dissected from 5–6 embryos of mixed sex and pooled for a single replicate culture. Trypsin (0.25%) was used to dissociate tissue through a 10-min incubation at 37°C. Digestion was terminated with the addition of ovomucoid (trypsin inhibitor, Worthington). Digested tissue was gently triturated through a P1000 pipette to release cells and passed through a 40 μm filter. After trituration, the cell suspension was transferred to a 15 ml Falcon tube and centrifuged for 5 min at RT/154 × *g*. After centrifugation, the cloudy supernatant was carefully removed with a pipette and discarded. The pellet was resuspended in 10 ml DMEM medium and added to uncoated 90 mm Petri dishes. The plates were incubated at 37°C in 5% CO_2 humidified incubator for 30 min. During this incubation, glial cells and other unwanted debris adhere to the bottom of the plate while cortical cells are retained in the media and recover from the trituration. The supernatant was carefully removed, without disturbing attached glial cells and unwanted cell debris at the bottom of the plate, and moved into a new 15 ml Falcon tube using a pipette. The collected supernatant was then centrifuged for 5 min at RT/154 × *g*. Neurons were plated onto cell culture dishes pre-coated overnight with poly-d-lysine (20 μg/ml) and laminin (4 μg/ml) and were grown in neurobasal medium (Gibco) containing B27 supplement (2%), 1% PenStrep solution, and glutaMAX (1 mM). Neurons were grown in incubators maintained at 37°C with a CO_2 concentration of 5%. GapmeRs for unassisted uptake were added directly to the culture medium at a final concentration of 500 nM, and the neurons were cultured for a total of 10 days.

Neuronal images were acquired at 10× magnification on an ImageXpress Micro (Molecular Devices) automated microscopy system and quantified using WIS-Neuromath [28]. The parameters reported include total outgrowth, defined as the sum of lengths of all processes and branches per cell, the number of processes, the average process length, and the number of branching points. N2a cells were seeded onto multiwell plates coated with poly-D-lysine (20 μg/ml) and laminin (4 μg/mL) and differentiated as described below. Images were acquired at 10× magnification using an EVOS Cell Imaging System (Thermo Fisher Scientific) and quantified using WIS-Neuromath.

Plasmid construction

The sequence corresponding to the complementary DNA (cDNA) of mouse *Bahcc1* (ENSMUST00000118987) without the stop codon was synthesized by Hylabs and cloned inside the pLIX_402 vector (gift from David Root, Addgene #41384) by PCR cloning via 5′ NheI and 3′ AgeI sites by recombination. To generate a plasmid encoding a full-length *Bahcc1* without the BAH domain (Bahcc1$^{\Delta BAH}$-HA), we digested the plasmid with AgeI to remove the last 918 bp of the *Bahcc1* CDS. All plasmids were sent for Sanger and whole plasmid sequencing (Plasmidsaurus) prior to use.

Sodium butyrate, romidepsin, and retinoic acid treatments

Sodium Butyrate (Sigma) was diluted in sterile H_2O at a stock concentration of 1M and added to the cell culture media at a final concentration of 5 μM. Romidepsin (Sigma) was diluted in tissue culture-grade DMSO at a stock concentration of 10 mM and further diluted in cell media at a final concentration of 5 nM. As controls, cells were supplemented with an equal volume of H_2O (sodium butyrate) or DMSO (romidepsin). Both treatments were performed for 24 h in order to minimize indirect effects due to the extensive inhibition of deacetylation. Retinoic acid (RA) (Sigma) was diluted in DMSO at a stock concentration of 0.01M and added to complete media with reduced (1%) serum concentration at a final concentration of 10 μM, with equal volumes of DMSO serving as vehicle controls. After 3 days of treatment, cells were transfected with GapmeRs as previously described and incubated for three additional days in the RA medium.

Gene expression analysis by RT-qPCR

RNA was extracted by using TRI-Reagent, according to the manufacturer's instructions. Briefly, cells were washed once with 1× phosphate bufferedsaline (PBS) and the proper amount of TRI was added directly to the wells. After complete lysis, 200 μL of chloroform for each mL of TRI was added, and the samples were centrifuged at 4°C/15 000 rpm for 15 min, and the resulting upper aqueous phase was isolated. RNA was then precipitated by adding 500 μL of 2-propanol for each ml of TRI, incubated at room temperature for 15 min while rotating, and centrifuged for 15 min at 4°C/15 000 rpm. The RNA pellet was then washed once with 1 ml of 75% ethanol and dried. RNA was resuspended in DNase/RNase-free H_2O. Baseline-ZERO™ DNase (Biosearch Technologies) was applied to 1–2 μg of total RNA, following the manufacturer's recommendations and incubating for 1 h at 37°C. DNase-treated or untreated RNA was retrotranscribed using the qScript™ Flex cDNA Synthesis Kit (Quanta Bio), with either oligo-dT or a 1:1 combination of oligo-dT and random hexamers, following standard conditions as suggested by the manufacturer. The resulting cDNA was then diluted 1:5–1:10 with DNase/RNase-free H_2O and used as input for quantitative real-time PCR using the Fast SYBR™ Green Master Mix (Applied Biosystems). Each reaction (5 μl Fast SYBR™ Green Master Mix, 1 μl diluted cDNA, 3.75 μl DNase/RNase-free H_2O and 0.25 μl of 10 μM forward + reverse primers) was carried out in triplicate and amplified using the following PCR program: 20 s at 95°C, 40 cycles by denaturing for 1 s at 95°C followed by annealing/extension for 20 s at 60°C. Results were analyzed using the ΔΔCt method. The complete list of primers and their sequences is available in Supplementary Table S1.

Protein extraction and western blot

Proteins were extracted using RIPA buffer [150 mM NaCl, 1% NP-40, 0.5% deoxycholate, 0.1% sodium dodecyl sulfate (SDS), 50 mM TRIS, pH 8, 1 mM Dithiothreitol (DTT)], freshly supplemented with EDTA-free Protease Inhibitor Cocktail (APExBIO). Briefly, cells were detached with a trypsin (0.05%)–EDTA (0.02%) solution, pelleted by centrifugation, resuspended in ice-cold RIPA buffer, and incubated on ice for 20 min with occasional vortexing. The lysates were then centrifuged at 15 000 rpm for 15 min at 4°C, and the supernatants were collected, quantified by Bradford assay, and stored at −80°C. To isolate histones, the cells were directly lysed in 1× Laemmli sample buffer [29], followed by three cycles of boiling at 95°C for 5 min and vortexing for 30 s. For western blots, an equal amount of proteins was loaded on a polyacrylamide gel and run in SDS running buffer. Proteins were then transferred to a pre-activated 0.2 or 0.45 μm PVDF membrane in a cold Tris-Glycine buffer supplemented with 20% methanol inside ice, with a constant current of 0.30 A for 2 h. Blocking was done in 5% milk in 1× PBS-0.1% Tween 20 for at least 1 h, after which the membranes were incubated O/N at 4°C with the primary antibodies diluted in 5% milk in 1× PBS-0.1% Tween 20. The following day, the membranes were washed three times with 1× PBS-0.1% Tween 20, incubated for 2 h at RT with the appropriate secondary antibodies in 5% milk in 1× PBS-0.1% Tween 20, and washed again three times prior to image acquisition. Images were then quantified with Image Lab. The complete list of primary and secondary antibodies and relative dilutions is available in Supplementary Table S1.

Co-immunoprecipitation

A total of 5−10 × 10^6 cells were detached with a trypsin (0.05%)–EDTA (0.02%) solution, pelleted by centrifugation and frozen at −80°C for at least 1 h. The pellets were then thawed, resuspended in 450 μl of ice-cold lysis buffer (1% Triton X-100, 50 mM Tris–HCl, pH 7.4, 150 mM NaCl) freshly supplemented with EDTA-free Protease Inhibitor Cocktail (APExBIO) and incubated on ice for 20 min with occasional vortexing. For each sample, 50 μl of Protein A/G paramagnetic beads were washed three times with ice-cold lysis buffer, and resuspended in 250 μl of ice-cold lysis buffer. The lysates were then centrifuged at 15 000 rpm for 10 min at 4°C, the supernatants were collected into a new tube and pre-cleared with 50 μl of unconjugated beads for ∼30 min at RT, while gently rotating. The rest of the beads were incubated with 5 μg of antibody for ∼1 h at RT with gentle rotation, after which they

were washed again three times with ice-cold lysis buffer to remove any excess antibody, and finally incubated with the precleared protein lysates overnight at 4°C while gently rotating. The following day, the beads were washed three times with ice-cold lysis buffer to remove unbound proteins. For western blot analysis, the beads were eluted directly in a loading buffer and incubated for 5 min at 95°C, and the eluate was either stored at –80°C or directly loaded on a gel. For liquid chromatography mass spectrometry (LC-MS), the beads were eluted in 25 µl of 50 mM Tris–HCl (pH 7.4) supplemented with 5% SDS and incubated for 10 min at RT, and the eluate was stored at –80°C. The complete list of antibodies and relative dilutions is available in Supplementary Table S1.

Sample preparation, LC-MS, and data processing

The samples were subjected to tryptic digestion using an S-trap [30]. The resulting peptides were analyzed using nanoflow liquid chromatography (Acquity M-Class) coupled to high-resolution, high-mass-accuracy mass spectrometry (Exploris 480 for N2a samples, Q Exactive HFX for HEK293T samples). Each sample was analyzed on the instrument separately in a random order in discovery mode.

N2a raw data were processed with FragPipe v22. The data were searched in MSFragger search engine against the murine SwissProt proteome database appended with common lab protein contaminants and the following modifications: carbamidomethylation of C as a fixed modification and oxidation of M and protein N-terminal acetylation as variable ones. The protein intensities were extracted and used for further calculations using Perseus v1.6.2.3. The intensities were $\log_2$ transformed, and only proteins that had at least two valid values in at least one experimental group were kept. The remaining missing values were imputed. A Student's *t*-test was performed to identify the proteins that are differentially expressed. HEK293T raw data were processed with MetaMorpheus v1.0.2. The data were searched against the human UniProt proteome database (xml version including known PTMs) appended with the BAHCC1-HA sequence, common lab protein contaminants, and the following modifications: carbamidomethylation of C as a fixed modification and oxidation of M as a variable one. Quantification was performed using the embedded FlashLFQ [31] and protein inference [32] algorithms. The LFQ (label-free quantification) intensities were calculated and used for further calculations using Perseus v1.6.2.3. Decoy hits were filtered out. The LFQ intensities were log transformed and only proteins that had at least two valid values in at least one experimental group were kept. The remaining missing values were imputed. A student's t-test was performed to identify the proteins that are differentially expressed.

Cleavage under targets and release using nuclease

Cleavage under targets and release using nuclease (CUT&RUN) reactions were performed following the V3 of the protocol [33], with minor modifications. An equal number of cells (up to 500 000 for each sample/replicate) was harvested using a trypsin (0.05%)–EDTA (0.02%) solution and washed once with 1× PBS at room temperature. After three washes with Wash Buffer [20 mM HEPES-NaOH, pH 7.5, 150 mM NaCl, 0.5 mM Spermidine supplemented with EDTA-free Protease Inhibitor Cocktail (APExBIO)] at RT, cells were resuspended in 1 ml Wash Buffer and incubated while gently rotating with 20 µl of Concanavalin A-coated magnetic beads (EpiCypher), which have been previously washed, activated and resuspended with Binding Buffer (20 mM HEPES-NaOH, pH 7.5, 10 mM KCl, 1 mM $CaCl_2$, 1 mM $MnCl_2$). After 10′, the buffer was removed, and the beads were resuspended in 150 µl of Antibody Buffer (Wash Buffer with 0.1% Digitonin (Sigma) and 2 mM EDTA, pH 8) containing the proper dilution of the antibody of interest and left gently rotating overnight with a 180° angle at 4°C. On the next day, cells were washed two times with ice-cold Dig-Wash Buffer (Wash Buffer with 0.1% Digitonin), resuspended in 150 µl of Dig-Wash Buffer supplemented with 1 µl of custom-made pA/G-MNase every ml and left rotating for 1 h at 4°C. After that, cells were washed again two times with Dig-Wash Buffer, resuspended in 100 µl of Dig-Wash Buffer, and placed into a thermoblock sitting on ice. To initiate the cleavage reaction, 2 µl of a freshly diluted (from a 1M stock) solution of 100 mM $CaCl_2$ was added to each tube, and the tubes were left at 0°C for 30 min. To halt the reaction, 100 µl of 2× STOP Buffer (340 mM NaCl, 20 mM EDTA, pH 8, 4 mM EGTA, pH 8, 0.05% Digitonin, 100 µg/ml RNAse A, 50 µg/ml Glycogen) were added to each tube, and cleaved DNA fragments were released by incubating the samples for 30′ at 37°C. The tubes were then centrifuged for 5 min at 4°C/16 000 × *g* and the supernatant was collected. Finally, the DNA was purified by standard phenol/chloroform extraction using the 5PRIME Phase Lock Gel Heavy tubes (QuantaBio), and the success of the CUT&RUN reaction was assessed by running the positive control (H3K27me3 or H3K4me3) on a Tapestation (Agilent Technologies) using a High Sensitivity D1000 ScreenTape (Agilent Technologies). When using the H3K27ac, SIN3A, SIN3B, and BAHCC1 antibodies, all buffers were supplemented with 20 mM of sodium butyrate (Sigma) to prevent the loss of acetylated residues. The complete list of primary and secondary antibodies and relative dilutions is available in Supplementary Table S1.

To perform CUT&RUN-qPCR, the purified DNA was further diluted 1:2 in DNase/RNase-free H_2O and 1 µl was used as input for qPCR as described above. For each tested gene, we designed a set of primers targeting the BAHCC1-bound region [i.e. Transcriptional Start Site (TSS)] and another set targeting a region where BAHCC1 was not predicted to bind (i.e. genebody). Each gene/region was normalized on the same region of the negative control (i.e. *Gapdh*), after which the $2^{-\Delta Ct}$ was calculated. Lastly, we computed the ratio between the $2^{-\Delta Ct}$ of the TSS and that of the genebody as a proxy of enrichment of the predicted binding site versus the nearby genomic landscape.

RNA-seq and CUT&RUN library preparation

RNA-seq libraries were prepared using the CORALL mRNA-Seq Kit V2 (Lexogen), following the manufacturer's instructions. Prior to library generation, 1 µg of total RNA was PolyA-enriched using the Poly(A) RNA Selection Kit V1.5 (Lexogen). To prepare CUT&RUN libraries, we followed the original protocol [33], with slight modifications. Briefly, to 30 µl of purified CUT&RUN DNA, we added 10 µl of a 4× End Repair and A-Tailing (ERA) Buffer, consisting of 4 µl of 10× T4 DNA Ligase Buffer (NEB), 2 µl 10 mM dNTPs mix, 1 µl 10 mM ATP, 2 µl of 50% PEG 4000 (Thermo Fisher Scientific), 0.6 µl PNK (NEB), 0.1 µl T4 DNA Polymerase (NEB), and 0.3 µl of Taq Polymerase (homemade). Samples were incu-

bated in a thermocycler preheated at 12°C with the following program: 15 min at 12°C, 15 min at 37°C, 45 min at 58°C, hold at 8°C. Barcoding was performed by adding to each sample 54 µl of 2X DNA Quick Ligase Buffer (NEB), 4 µl of DNA Quick Ligase (NEB) and 10 µl of unique Y-shaped adaptors (final concentration of 0.075 µM). The samples were incubated for 20′ in a preheated thermocycler at 20°C, after which 1 µl of 20% SDS and 2 µl of 20 mg/ml Proteinase K were added and the temperature was raised to 37°C for 1 h. Following purification with 1× SPRI beads (GE Healthcare) and a second round with 1.2X HXP Buffer (20% PEG 8000, 2.5M NaCl), libraries were amplified by a PCR reaction composed of 25 µl 2× KAPA HiFi HotStart ReadyMix (Roche), 2 µl of Primer Mix (Illumina TruSeq Universal and Illumina P7 standard primers, at 50 µM each) and 23 µl of purified DNA from the previous step, with a PCR program consisting of 45" at 98°C, 14 cycles of 15" at 98°C and 10" at 60°C, with a final extension of 1 min at 72°C. Amplified libraries were subsequently purified with 1.1X SPRI beads and then again with 1.2X HXP Buffer. The libraries were then quality-checked by both dsDNA Qubit (Thermo Fisher Scientific) and Tapestation (Agilent Technologies). All libraries were sequenced on an Illumina NovaSeq 6000 or Novaseq X instrument, aiming for either 10M (CUT&RUN) or 15M (polyA + RNA-seq) reads per sample.

RNA-seq data analysis

Raw FASTQ files were processed by an adapted Lexogen CORALL analysis pipeline script (https://github.com/Lexogen-Tools/corall_analysis). Briefly, adaptors were trimmed by using Cutadapt [34], and the resulting trimmed FASTQ files were used as input for mapping to the mm10 mouse genome with STAR aligner [35], using the `–quantMode GeneCounts` option in order to count the number of reads mapping to each feature provided by an appropriate GTF file. To call for differential expression, we used DESeq2 [36], considering a gene to be differentially expressed when adjusted $P < 0.05$ and absolute $\log_2$FC > 0.41 (∼33% increase or decrease). Prior to any subsequent analysis, we filtered out poorly expressed genes, pseudogenes, and genes with an exonic length <200 nt. To perform GO enrichment analysis and GSEA, we used the Clusterprofiler R package [37] by considering a term to be enriched when the adj. $P < .05$. Whenever several redundant terms were found, we employed the *simplify* function with a cutoff = 0.7 to reduce the redundancy.

CUT&RUN data analysis

Raw FASTQ files were aligned to the mm10 reference genome with Bowtie2 [38], using the -p 8, -X 2000, and –nounal options. BAHCC1 and SIN3A peaks were called using the MACS2 callpeak function [39], whereas for H3K27ac, H3K4me3, and H3K27ac we instead used epic2 [40]. Peak quantification and differential expression were performed using the HOMER tool suite [41], using the *annotatePeaks.pl* and *getDiffExpression.pl* functions, respectively. To calculate the extent of the overlap between BAHCC1, H3K27ac, and H3K4me3 peaks, we employed BEDTools intersect tool [42]. To compute the correlation between individual bigWig files and to plot the metagene profiles and coverage heatmaps, we employed *bigWigCorrelate* and deepTools [43], respectively.

Immunostaining

Cells were plated and transfected on either sterile glass coverslips or eight-well chambers (Ibidi). Cells were first washed once with 1× PBS, and then fixed with cold 4% PFA in 1× PBS for 15 min at RT. After two washes with 1× PBS for 5 min each, cells were permeabilized by incubating them with 5% horse serum, 1 mg/ml Bovine Serum Albumin (BSA), 0.1% Triton-X100 in 1× PBS for 30 min at RT. Following three washes with 1× PBS at RT, cells were incubated O/N at 4°C with the primary antibodies in blocking solution (5% horse serum, 1 mg/ml BSA in 1× PBS). The day after, cells were washed three times with 1× PBS and incubated for 2 h at RT with the secondary antibodies in a blocking solution, protected from light. Lastly, cells were washed three times with 1× PBS, stained with DAPI, and mounted with ProLong™ Glass Antifade Mountant (Invitrogen). Slides were left curing in the dark O/N at RT and eventually imaged with a Zeiss Spinning Disk confocal microscope. The complete list of primary and secondary antibodies and relative dilutions is available in Supplementary Table S1.

Wound healing assay and analysis

To perform the wound healing assay, we employed the µ-Plate 24 Well system (Ibidi) in order to increase consistency between scratches and standardize the experimental conditions. Moreover, to avoid the need to detach and plate again cells that already underwent transfection, we introduced the targeting and control GapmeRs via reverse transfection, employing the same conditions as in the regular settings and diluting the transfection mixes directly into the cell mixtures while seeding. A total of six replicates for each condition were seeded and transfected. After reaching confluence overnight, the culture inserts were gently removed with sterile forceps, and the wells were washed with 1× PBS to remove any cell debris. Brightfield images were taken using an EVOS Cell Imaging System (Thermo Fisher Scientific) at different time points. Data analysis was then performed using the Wound_healing_size_tool [44] plugin for ImageJ, which calculates the total (µm^2) and percentage (%) of the wounded area. From these data, we calculated the percentage of wound closure as follows:

$$\text{Wound Closure } (\%) = \frac{A_{t=0} - A_{t=\Delta t}}{A_{t=0}}.$$

With $A_{t=0}$ and $A_{t=\Delta t}$ being the wounded area (in µm^2) at the beginning and after time t, respectively. The raw and normalized (on time 0) area were also used as parameters, given the highly standardized experimental setting.

Transwell assay

To measure cell migration, we performed a transwell invasion/migration assay using transwell inserts with 8.0 µm pores (Corning). Briefly, cells were plated and reverse transfected as described above in low-serum (1%) media on the upper part of each insert. In the bottom part, we added regular media (10% serum) in order to attract the cells. After 24 h, non-migrated cells were scraped off using sterile cotton swabs, after which the wells were washed three times with 1× PBS. The migrated cells on the lower part were then fixed with ice-cold 4% PFA for 15 min at room temperature, washed twice with 1× PBS, and stained with crystal violet for 10 min, after which they were washed two more times with 1× PBS. Crystal

violet was then extracted by adding a 33% acetic acid solution for 10 min while gently rocking the plate. Finally, optical density at 595 nm was measured using a Cytation 5 microplate reader (BioTek).

Results

Bahcc1 binds active regulatory regions in a neuronal cell line

To characterize the roles of BAHCC1 in cells of a neuronal lineage, we used the mouse Neuro2a (N2a) neuroblastoma cell line, which is readily transfectable, thus permitting transient manipulations and large-scale biochemical and genomic assays. We also employed a polyclonal antibody against BAHCC1 that we developed (Fig. 1A and Supplementary Table S1). We first assessed the specificity of this antibody by Western blot and immunofluorescence (IF) after *Bahcc1* knockdown (KD) with GapmeR antisense nucleotides and overexpression (OE) by transfection of a plasmid encoding an HA-tagged full-length *Bahcc1* coding sequence (CDS). These experiments show that the BAHCC1 signal, as reported by the antibody, responds to changes in *Bahcc1* levels (Fig. 1A, left), and that its staining overlaps that of HA in transfected cells (Fig. 1A, right). To profile BAHCC1 genomic occupancy, we performed a CUT&RUN [33] assay using the antibody for the endogenous protein in untransfected cells (UT) or an anti-HA antibody in cells expressing an HA-tagged Dox-inducible full-length BAHCC1 protein (OE). Both experiments revealed overall concordant binding profiles ($\rho = 0.48$, $P < 10^{-15}$, Fig. 1B) with enrichment in similar regions, suggesting that BAHCC1 overexpression and tagging do not strongly affect its genome-wide occupancy (Supplementary Fig. S1A–D). However, the pattern of the specific enrichment around the transcription start sites differed, as the endogenous BAHCC1 appeared most enriched in the regions immediately flanking the TSS, whereas the exogenously expressed one appeared most enriched at the TSS itself. These differences may reflect either the ability of the overexpressed protein to bind to regions that are less accessible to the endogenous one or differences in accessibility of fragments of the protein to the two different antibodies used.

We then further characterized the binding pattern of the endogenous protein. BAHCC1 was enriched immediately upstream and downstream to the TSS of active genes (Fig. 1C and Supplementary Table S2), in agreement with its profile in melanoma cells [17]. BAHCC1 CUT&RUN read coverage was slightly more prominent among promoters of more highly expressed genes (Fig. 1C) and largely absent around those not expressed in N2a cells, suggesting a role in regulating gene expression. We also profiled the canonical chromatin marks H3K27ac, H3K4me3, and H3K27me3 in untransfected N2a cells and found that BAHCC1 peaks were enriched with both H3K4me3 and H3K27ac (Fig. 1D and E), displaying a slightly higher relative signal for the latter. Specifically, we found that out of the 46,106 BAHCC1 peaks, 79.9% overlapped a H3K27ac peak and only 61.3% overlapped H3K4me3 peaks. On the contrary, BAHCC1 peaks were largely devoid of H3K27me3, in contrast to a recent report suggesting BAHCC1 is a reader of this chromatin mark [16]. Because of the association of BAHCC1 with SIN3A complex members in other cell lines [13, 16, 23–26], we profiled SIN3A and SIN3B occupancy in N2a cells by CUT&RUN. We found that SIN3A and BAHCC1 share a similar binding profile (Fig. 1D and E), whereas SIN3B was only mildly enriched in these regions. Both BAHCC1 and SIN3A were more strongly associated with H3K27ac-marked regions, with BAHCC1 displaying a preference for intergenic regions (Fig. 1F, top) and SIN3A for promoter-associated ones (Fig. 1F, bottom). When considering the genome-wide CUT&RUN read coverage, BAHCC1 showed the strongest correlation with H3K27ac and SIN3A/B, a moderate correlation with H3K4me3, and minimal correlation with H3K27me3 (Fig. 1G), consistent with our previous observations from the metagene profiles. The high correlation between BAHCC1 and SIN3B possibly results from the low coverage of the two proteins across many genomic regions and suggests that while SIN3B signal around BAHCC1 binding sites is negligible compared to SIN3A, it is also likely not particularly enriched in other regions (Fig. 1E). Overall, BAHCC1 chromatin occupancy suggests that it is associated with regions marked with acetylated histones and the SIN3A complex, and this association increases with increasing expression levels of associated genes.

BAHCC1 regulates gene expression in neuronal cells

To study the effect of BAHCC1 dosage, we perturbed BAHCC1 expression by different methods and quantified changes in gene expression by polyA(+) RNA-seq (Supplementary Table S3). Specifically, we knocked down *Bahcc1* in N2a cells using GapmeRs [45]—antisense oligonucleotides that trigger RNA degradation via nuclear RNAse H activity (Figs 1A and 2A)—as we found this approach to be more effective than siRNAs for depleting *Bahcc1* mRNA in N2a cells (Supplementary Fig. S2A and B). Furthermore, we knocked down *Bahcc1* in two different cellular states—undifferentiated N2a cells and cells differentiated into a more mature phenotype by a RA treatment [46] for 72 hrs (Supplementary Fig. S3A). We have also overexpressed *Bahcc1* in undifferentiated cells by transient transfection of a plasmid encoding an HA-tagged *Bahcc1* CDS (*Bahcc1-HA*, Figs 1A and 2B). We then analyzed changes in gene expression in these conditions using DeSeq2 [36], considering a gene to be differentially expressed if its adjusted $P < 0.05$ and it changed by at least 33% ($|\log_2 FC| > .41$). As expected, RA-mediated differentiation caused substantial transcriptomic changes (Supplementary Fig. S3B), with an increase in the expression of genes associated with neuronal maturation processes (Supplementary Fig. S3C), and a decrease in those associated with cell adhesion, migration, and proliferation (Supplementary Fig. S3D). Among the upregulated genes, several were related to the biogenesis, transport and release of dopamine, a feature previously observed in N2a cells [47].

We then focused on genes that were dysregulated after perturbing *Bahcc1* levels. Genes upregulated following *Bahcc1* KD in either (+)RA or (−)RA cells were enriched for processes related to stress response and immune activation (Fig. 2C and Supplementary S3E), whereas downregulated genes were strongly linked to neuronal development, maintenance, and functions (Fig. 2D and Supplementary S3F). Genes that were significantly upregulated after RA treatment and downregulated after *Bahcc1* KD in (+)RA cells (i.e. genes that fail to be properly activated by the differentiation process) are enriched in several processes related to neuronal

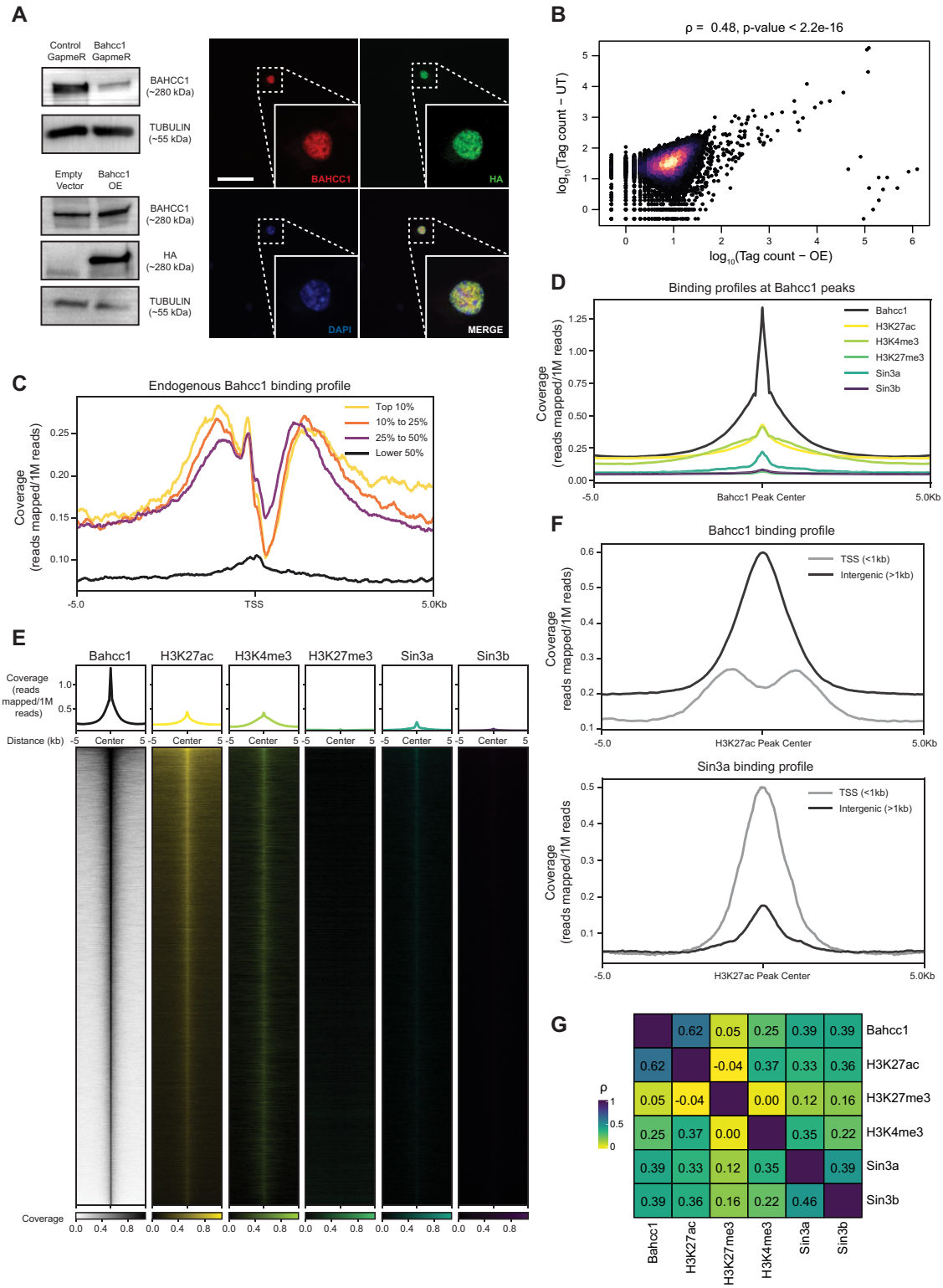

Figure 1. BAHCC1 chromatin occupancy in N2a cells. (**A**) Left: Western blots using the polyclonal BAHCC1 antibody developed in this study upon *Bahcc1* KD and OE. Staining reveals a decrease and an increase of BAHCC1 upon KD and OE, respectively, whereas HA is visible only upon transfection of the *Bahcc1-HA* plasmid. Right: IF showing co-localization of the BAHCC1 antibody signal with the HA-tag (scale bar = 30 μm, 60× magnification). (**B**) Correspondence between BAHCC1 CUT&RUN signals in untransfected (UT) and *Bahcc1*-overexpressing (OE) N2a cells. Each point is a binding peak detected by combining all the data; the *X*-axis depicts the number of reads in OE cells, and the *Y*-axis the number of reads in untransfected (UT) cells. Color indicates local point density. (**C**) Metagene profile around TSS of the normalized endogenous BAHCC1 CUT&RUN signal in N2a cells, stratified by gene expression levels. (**D**) Metagene profiles of normalized CUT&RUN signals of H3K4me3, H3K27ac, SIN3A, and SIN3B, centered over BAHCC1 peaks. (**E**) Heatmap of read coverage around the BAHCC1 peaks, ranked by BAHCC1 binding and centered around the peak. Coverage and heatmaps of BAHCC1, H3K27ac, H3K4me3, H3K27me3, SIN3A, and SIN3B are shown. (**F**) Metagene profiles of normalized CUT&RUN signals of endogenous BAHCC1 (top) and SIN3A (bottom), centered over H3K27ac TSS-associated (<1 kb) or intergenic (>1 kb) peaks. (**G**) Heatmap for the correlations of the CUT&RUN coverage between the examined proteins and histone modifications. Colors and numbers represent the Spearman's correlation coefficients.

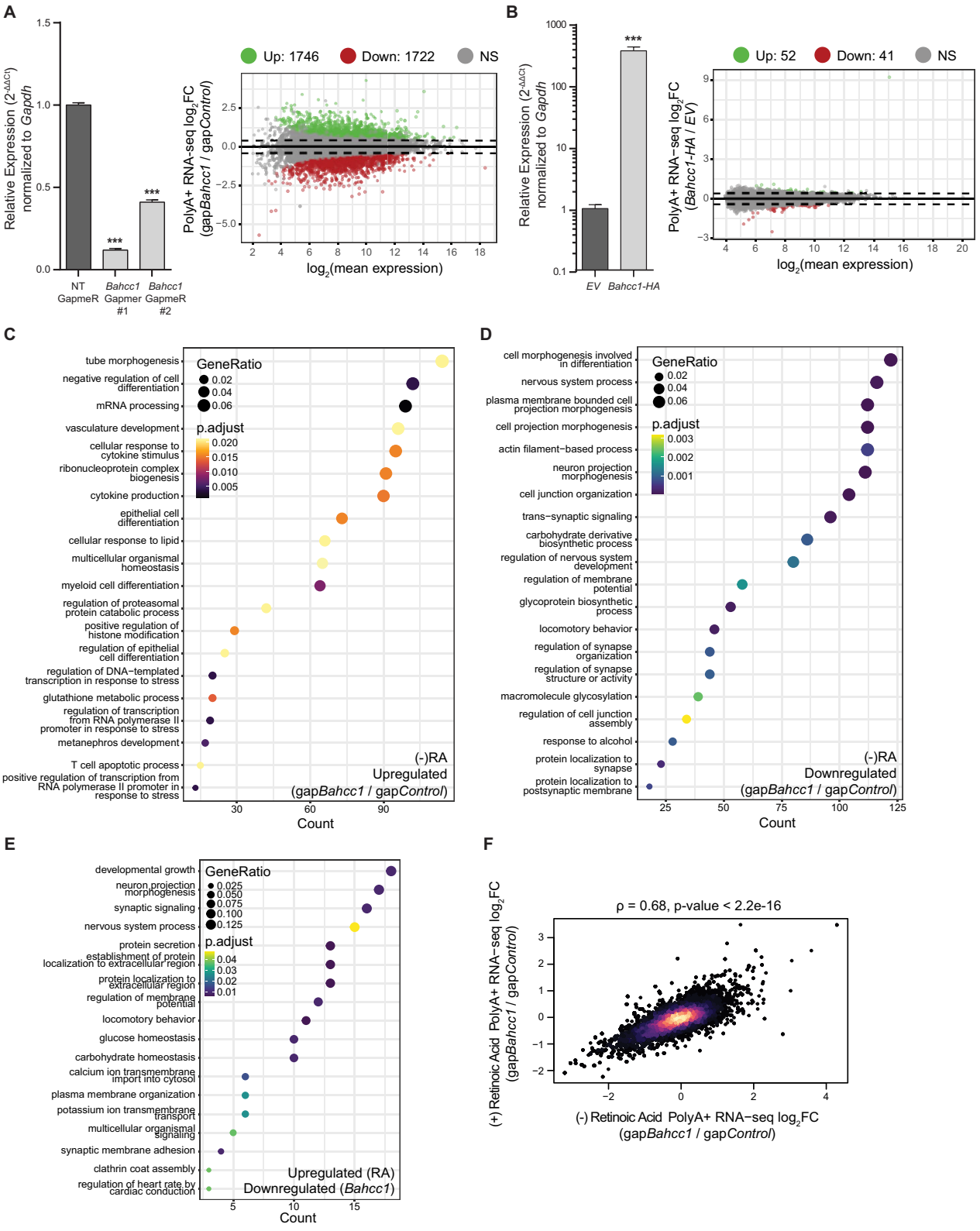

Figure 2. Genome-wide transcriptomic changes upon BAHCC1 perturbations. (**A**) RT-qPCR upon *Bahcc1* depletion with GapmeRs to assess KD efficiency (left) and an MA plot showing the changes in genome-wide gene expression (right). (**B**) RT-qPCR upon transient transfection of a plasmid encoding *Bahcc1* CDS with a C-terminal HA-tag to assess OE efficiency (left), and MA plot showing the changes in genome-wide gene expression (right). (**C**) GO enrichment analysis of the upregulated genes following *Bahcc1* KD with GapmeRs in undifferentiated cells. (**D**) Same as panel (C), but for the downregulated genes. (**E**) GO enrichment analysis of genes normally upregulated by RA treatment but instead repressed by *Bahcc1* depletion with GapmeRs during differentiation. (**F**) Correspondence between changes in gene expression after *Bahcc1* KD with GapmeRs in (−)RA and (+)RA N2a cells. Color indicates local point density. All experiments were performed in $n = 3$ biological replicates, with the error bars in the barplots representing the standard deviation, $P > .05$ = ns; $< .05$ = *, $< .01$ = **; $< .001$ = *** (two-tailed Student's *t*-test). Genes were considered to be differentially expressed when adj. $P < .05$ and $|\log_2 FC| > .41$ (corresponding to a change of 33%).

morphogenesis, synapsis development, and signaling (Fig. 2E), hinting that BAHCC1 activity could be related to neuronal differentiation. However, gene expression changes following *Bahcc1* KD before and after differentiation were broadly similar (Fig. 2F), suggesting that BAHCC1 regulates a shared set of genes regardless of the cellular state. Thus, in subsequent analysis, we focused on changes in gene expression in undifferentiated cells. Overexpression of HA-tagged *Bahcc1* had modest effects on gene expression (Fig. 2B). The upregulated genes were enriched for immune activation and cellular proliferation (Supplementary Fig. S3G), whereas the downregulated ones were involved in general RNA processing (Supplementary Fig. S3H). These results indicate that perturbing BAHCC1 levels triggers substantial changes in N2a cells that are consistent between undifferentiated and differentiated cells, affecting genes important for neuronal development, maintenance, and function. Notably, since *Bahcc1* OE has more modest effects compared to its KD, endogenous levels of BAHCC1 in N2a cells appear to suffice to exert its functions.

The enrichment of cell locomotion-associated genes among the genes downregulated following *Bahcc1* KD and upregulated upon *Bahcc1* OE led us to examine cell migration and invasion in *Bahcc1* KD and OE cells. *Bahcc1* KD resulted in a marked reduction in the ability of N2a cells to bridge the gap in a wound healing assay (Supplementary Fig. S4A–C), as well as to migrate in a nutrient gradient as assessed in a transwell assay (Supplementary Fig. S4D). These effects of *Bahcc1* KD are consistent with those observed in melanoma cells, where *Bahcc1* KD led to reduced cell proliferation and invasion [17]. Conversely, *Bahcc1* OE cells demonstrated a higher capacity in filling the gap in wound healing experiments (Supplementary Fig. S4E–G), in agreement with its higher expression in various subtypes of melanoma compared to healthy tissues [17]. Notably, co-transfection of the *Bahcc1*-targeting GapmeR and *Bahcc1-HA* plasmid resulted in a full recovery of the migratory capabilities of N2a cells (Supplementary Fig. S4H), suggesting that these effects are BAHCC1-mediated. Prompted by the enrichment among the downregulated genes of neuronal morphology and synapse-related genes, we further analyzed the morphology of differentiated N2a cells following *Bahcc1* KD using WIS-Neuromath software [28] (Supplementary Fig. S5A). We did not observe any appreciable difference in branching complexity, average process length nor number of branches and branching points (Supplementary Fig. S5B), although we note that differentiated N2a cells differ from mature neurons and exhibit only short neurites with low complexity (Supplementary Fig. S5A). Taken together, these results indicate that BAHCC1 activity is required to establish a proper gene expression program in N2a cells, and its dysregulation causes decreased expression of neuronal lineage-commitment genes and altered cell motility.

BAHCC1 positively regulates gene expression by regulating H3K27ac levels at promoter-distal sites

To evaluate the effects of BAHCC1 on chromatin, we first examined the effect of BAHCC1 perturbations on global H3K27ac, H3K4me3, and H3K27me3 levels and found no overall differences, in contrast to the HDAC inhibitors sodium butyrate and romidepsin, which significantly increased global H3K27ac levels (Supplementary Fig. S6A and B). To examine changes at specific sites, we used CUT&RUN in biological triplicates to profile H3K27ac and H3K4me3 in *Bahcc1* KD and OE cells. We associated each of the 46 129 H3K27ac peaks we identified in N2a cells (Fig. 3A) with the nearest gene and used DeSeq2 to compute the effect of *Bahcc1* perturbations on each peak. Since changes in histone modification levels when examining KD or OE independently were overall modest, we focused on the difference between *Bahcc1* OE and KD (comparing each to their respective controls) and compared the changes in gene expression to changes in H3K27ac and H3K4me3. Changes in gene expression were significantly yet modestly correlated with changes in H3K27ac at the associated peaks ($R = 0.13$, $P < 10^{-15}$), whereas a substantially weaker correlation was observed for H3K4me3 ($R = -0.04$, $P = 7.2 \times 10^{-7}$). The association with H3K27ac was weaker yet still significant separately for the KD and the OE of BAHCC1 (KD: $R = 0.08$ and $P < 10^{-15}$; OE: $R = 0.04$ and $P = 8.9 \times 10^{-9}$).

We then focused specifically on genes that were differentially regulated by the BAHCC1 dosage and defined 553 "positively regulated" genes as those that were significantly ($P < .05$) increased by *Bahcc1* OE and significantly decreased by its KD and had a change of at least 33% following either OE or KD. Conversely, we defined 113 negatively regulated genes as those that decreased following the OE and increased following KD, with the same criteria. Positively regulated genes were strongly enriched in biological processes related to neuron development, projection guidance, adhesion, and synaptic signaling (Fig. 3B). In contrast, negatively regulated ones were not enriched in any biological process. These two gene sets were compared to 11 386 "not regulated" genes whose transcripts changed by <33%, with $P > .05$ in both OE and KD. BAHCC1 occupied peaks (when combining CUT&RUN from both endogenous and over-expressing cells) associated with positively regulated genes more than peaks associated with the negatively regulated ones or ones that were not regulated (Fig. 3C). The peaks associated with the positively regulated genes had reduced H3K27ac following *Bahcc1* KD (Fig. 3D), whereas *Bahcc1* OE increased H3K27ac in these regions (Fig. 3E). Peaks associated with negatively regulated genes were instead not significantly affected (Fig. 3D and 3E). BAHCC1 KD and OE led to significantly anti-correlated changes in H3K27ac at the peaks with the 10% strongest BAHCC1 binding ($R = -0.21$, $P < 10^{-15}$, Fig. 3F), whereas in the peaks in the bottom 50% of BAHCC1 binding the anti-correlation was much weaker ($R = -0.03$, $P = .005$, Supplementary Fig. S6C). This suggests that H3K27ac is more modulated by BAHCC1 levels at the regions most occupied by it, pointing to a direct involvement of BAHCC1 in the regulation of H3K27ac levels. H3K4me3 levels were affected only by Bahcc1 KD and exclusively in those peaks associated with the positively regulated genes (Supplementary Fig. S6D and E). No substantial anti-correlation was observed when considering H3K4me3 at BAHCC1-bound peaks ($R = -0.01$, $P = 0.36$), again primarily associating BAHCC1 with H3K27ac.

We then considered the 87 H3K27ac peaks near the positively regulated genes that increased by Bahcc1 OE ($P < .05$) or decreased by its KD ($P < .05$). We compared them to 366 peaks that did not change by 33% in either perturbation and 8,181 peaks near not-regulated genes ($P > .05$) in both conditions. The peaks in the first group exhibited higher levels of both BAHCC1 and SIN3A binding (Fig. 3G and Supplementary Fig. S6F), were broader (Fig. 3H), and

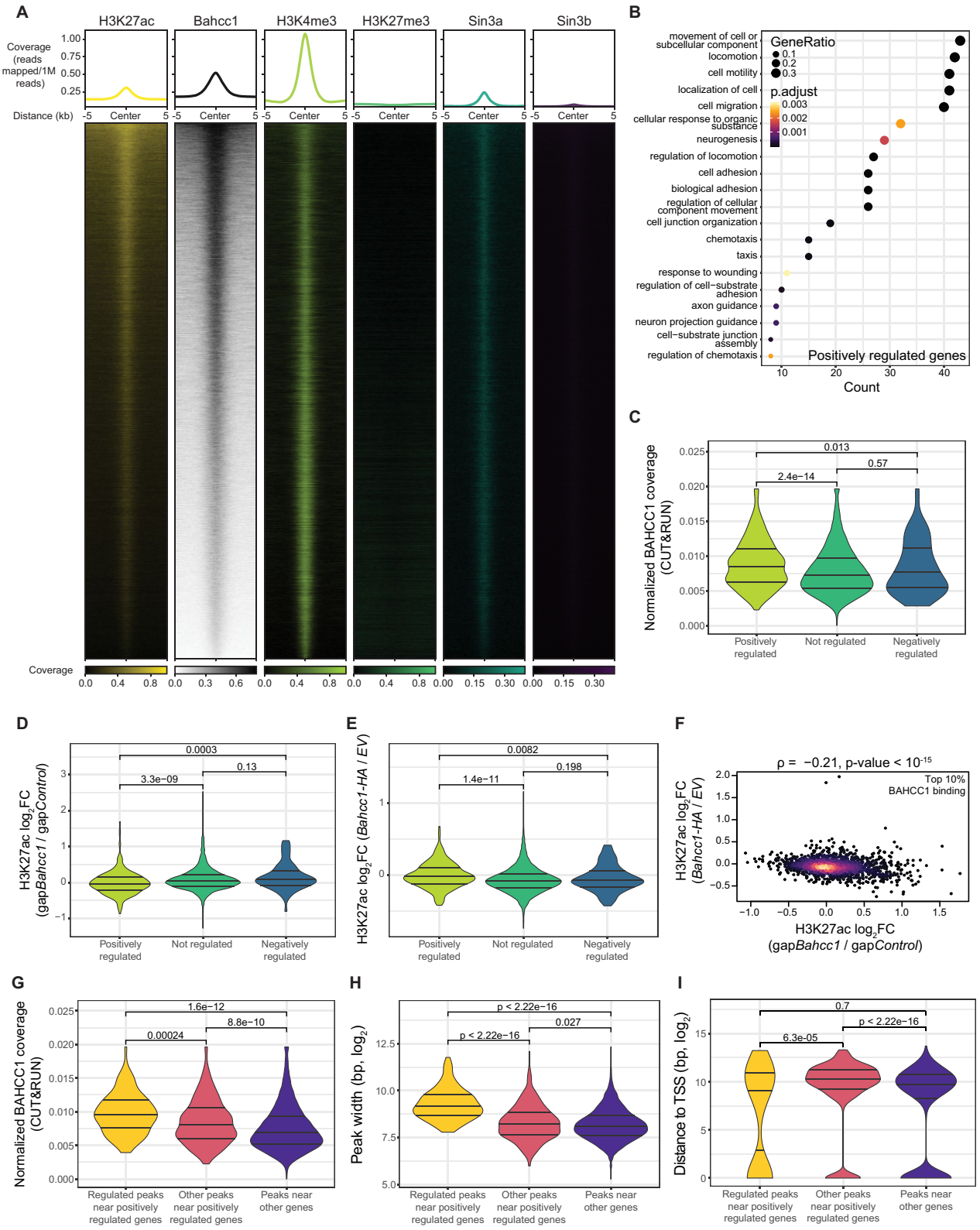

Figure 3. BAHCC1 positively regulates gene expression by affecting H3K27ac levels. (**A**) Heatmap of all high-confidence H3K27ac peaks, ranked by endogenous BAHCC1 coverage. Coverage of BAHCC1, H3K4me3, H3K27me3, SIN3A, and SIN3B, as well as their metagene profiles are shown. (**B**) GO enrichment of the positively regulated genes. (**C**) Normalized BAHCC1 CUT&RUN signal over H3K27ac peaks near positively, negatively, and unregulated genes. (**D**) Changes in H3K27ac at peaks near the BAHCC1-regulated genes in *Bahcc1* KD cells. (**E**) Same as in panel (D), but after *Bahcc1* overexpression. (**F**) Correspondence between changes in H3K27ac after *Bahcc1* KD and OE for the peaks with the top 10% average coverage of BAHCC1 CUT&RUN reads. Color indicates local point density. (**G**) Normalized BAHCC1 CUT&RUN signal over the H3K27ac-regulated peaks associated with the positively regulated genes. (**H**) Width (in log scale) of the regulated H3K27ac peaks. (**I**) Distance from the nearest TSS of the regulated H3K27ac peaks. In all violin plots, the three lines represent the median, first, and third quartiles, and significance of the different comparisons was calculated by using a Mann–Whitney test.

slightly closer to the transcription start sites compared to the other peaks associated with the positively regulated genes (Fig. 3I). Interestingly, positively regulated genes had lower SIN3A occupancy in their promoters compared to the other categories (Supplementary Fig. S6G). Notably, SIN3A occupancy is higher at promoters of highly transcribed genes, despite being considered a co-repressor given its involvement in SIN3–HDAC1 (Supplementary Fig. S6H). Interestingly, SIN3B occupancy also increases with gene expression levels (Supplementary Fig. S6I), but overall its genome-wide chromatin occupancy is much lower than that of SIN3A (Supplementary Fig. S6J), suggesting that in N2a cells is the latter the main scaffolding component of the SIN3–HDAC complexes. Nevertheless, SIN3B occupancy is higher, although lower than that of SIN3A, in the regulated H3K27ac peaks near positively BAHCC1-regulated genes (Supplementary Fig. S6K), but significantly lower in their promoters (Supplementary Fig. S6L), thus mimicking SIN3A behavior in these regions. We conclude that BAHCC1 primarily promotes gene expression, and changes in its levels are associated with changes in the H3K27ac mark in regions bound by BAHCC1.

BAHCC1 associates with SIN3A in neuronal cells independently of its BAH domain

Following the reported associations between BAHCC1 and SIN3A in other cell types [13, 16, 23–26], we wanted to further confirm this by native co-immunoprecipitation (co-IP) upon the transfection of the full-length Bahcc1-HA OE plasmid in N2a cells. Because the BAHCC1^{BAH} domain has been recently shown to be critical for its recruitment to chromatin and engagement with H3K27me3 in blood cells [16], we also generated and transfected a plasmid encoding an HA-tagged full-length *Bahcc1* lacking the last 918 nt of its CDS, which includes the BAH domain (*Bahcc1*$^{\Delta BAH}$*-HA*). HA staining revealed that we successfully pulled down BAHCC1, and staining with a SIN3A antibody validated the interaction for both WT BAHCC1 and BAHCC1-ΔBAH (Fig. 4A). To get an overview of the BAHCC1 interactome, we performed liquid chromatography followed by mass spectrometry (LC-MS) of the eluates from the co-IP using an anti-HA antibody after transfecting the cells with either the full-length *Bahcc1-HA*, *Bahcc1*$^{\Delta BAH}$*-HA*, or empty vector. A total of 84 and 56 proteins were found to be enriched (fold-enrichment > 1.5, $P < .05$) in the HA IP fraction after transfection with the full-length and Bahcc1$^{\Delta BAH}$-HA vectors, respectively, compared to the HA IP after transfection with the EV (Fig. 4B and C and Supplementary Table S4). Notably, SIN3A but not SIN3B was found to be enriched in both instances, and with the *Bahcc1*$^{\Delta BAH}$*-HA* vector, most other canonical SIN3A-HDAC subunits were also present (Fig. 4C). Moreover, loss of the BAH domain did not seem to have a major impact on the BAHCC1 binding profiles (Fig. 4D), suggesting that most of its protein–protein interactions do not require this domain. Enriched proteins were found to be involved in histone and protein acetylation/deacetylation (Fig. 4E), consistent with known functions and substrates of SIN3–HDAC and other HDAC complexes. Among the proteins recovered after pulling down the full-length BAHCC1, we detected the non-canonical SIN3–HDAC components OGT [13, 48, 49] and PHF23 [50], as well as TGS1, which was found to indirectly interact with SIN3A through their shared physical association with SMN [51]. We further confirmed these findings by transfecting the same vectors in the human HEK293T cell line, which, despite the interspecies difference, remarkably resulted in a more specific enrichment of SIN3A and other SIN3–HDAC subunits (Supplementary Fig. S7A–C), such as SAP130 and SUDS3. HDAC1 and HDAC2 were also found enriched in the presence of a full-length BAHCC1, but they were lost in the BAHCC1$^{\Delta BAH}$ mutant IP in HEK293 cells (Supplementary Fig. S7A–C). Taken together, these data highlight the physical association between BAHCC1 and SIN3A-HDAC, which is conserved when expressing the mouse BAHCC1 in human cells and does not depend on the BAH domain.

We further tested the colocalization of BAHCC1 with SIN3A, SIN3B, and different histone marks (H3K27ac, H3K4me3, and H3K27me3) by immunofluorescence. BAHCC1 (stained with an anti-HA antibody) was found exclusively in the nuclei of N2a cells, where it was co-localized with H3K4me3, H3K27ac, and SIN3A (Supplementary Fig. S8A). In contrast, we found again no evidence for co-localization of BAHCC1 with H3K27me3 (Supplementary Fig. S8A). Moreover, the deletion of the BAH domain did not affect BAHCC1 localization, which was still restricted to the nucleus (Fig S8A). Intrigued by this apparent dispensability of the BAH domain for BAHCC1 functions, we transfected the full length *Bahcc1-HA*, *Bahcc1*$^{\Delta BAH}$*-HA*, and empty vectors into N2a and performed again polyA(+) RNA-seq and compared the results with those obtained before (Fig. 2B). Overall, the global changes triggered by the two overexpressions were highly concordant (Supplementary Fig. S8B, $R = 0.56$, $P < 10^{-15}$), and despite all technical bias, well correlated with the previous OE experiment (Supplementary Fig. S8C, $R = 0.2$, $P < 10^{-15}$). We then compared the expression of the genes found to be differentially expressed in our previous experiment (Fig. 2B) to that of the same set of genes, but in our new sequencing datasets. Strikingly, the differentially expressed genes—either upregulated or downregulated—were significantly less dysregulated in the *Bahcc1*$^{\Delta BAH}$*-HA* samples compared to the full-length ones (Fig. 4F), hinting that the truncated protein is somewhat less functional.

We next tested if SIN3A also regulates the genes regulated by BAHCC1 by using siRNAs to deplete *Sin3a* in N2a cells (Fig. 4G). *Sin3a* KD promoted the expression of genes positively regulated by BAHCC1 (Fig. 4H). We then proceeded to KD other members of the SIN3–HDAC complex, specifically *Sin3b*, *Hdac1*, and *Fam60a* (Supplementary Fig. S9A–C). Interestingly, *Sin3b* KD had the opposite effect compared to *Sin3a*, with genes positively and negatively regulated by BAHCC1 being significantly reduced and induced by si*Sin3b*, respectively (Supplementary Fig. S9D), which resonates with potentially opposing functions of the two proteins in other systems (see "Discussion" section), and the specific association of BAHCC1 with SIN3A and not SIN3B. *Hdac1* and *Fam60a* KD had no significant effect on the positively regulated genes but did affect the negatively regulated ones (Supplementary Fig. S9E and F). To more efficiently inhibit HDAC activity, we treated N2a cells with sodium butyrate, a pan-HDAC inhibitor, resulting in large-scale gene expression changes (Supplementary Fig. S9G and H). Because sodium butyrate has a large spectrum of HDAC inhibitory action, we also treated N2a with romidepsin, a class I-specific HDAC inhibitor [52] that also triggered a massive transcriptional response (Supplementary Fig. S9I and J). Notably, these

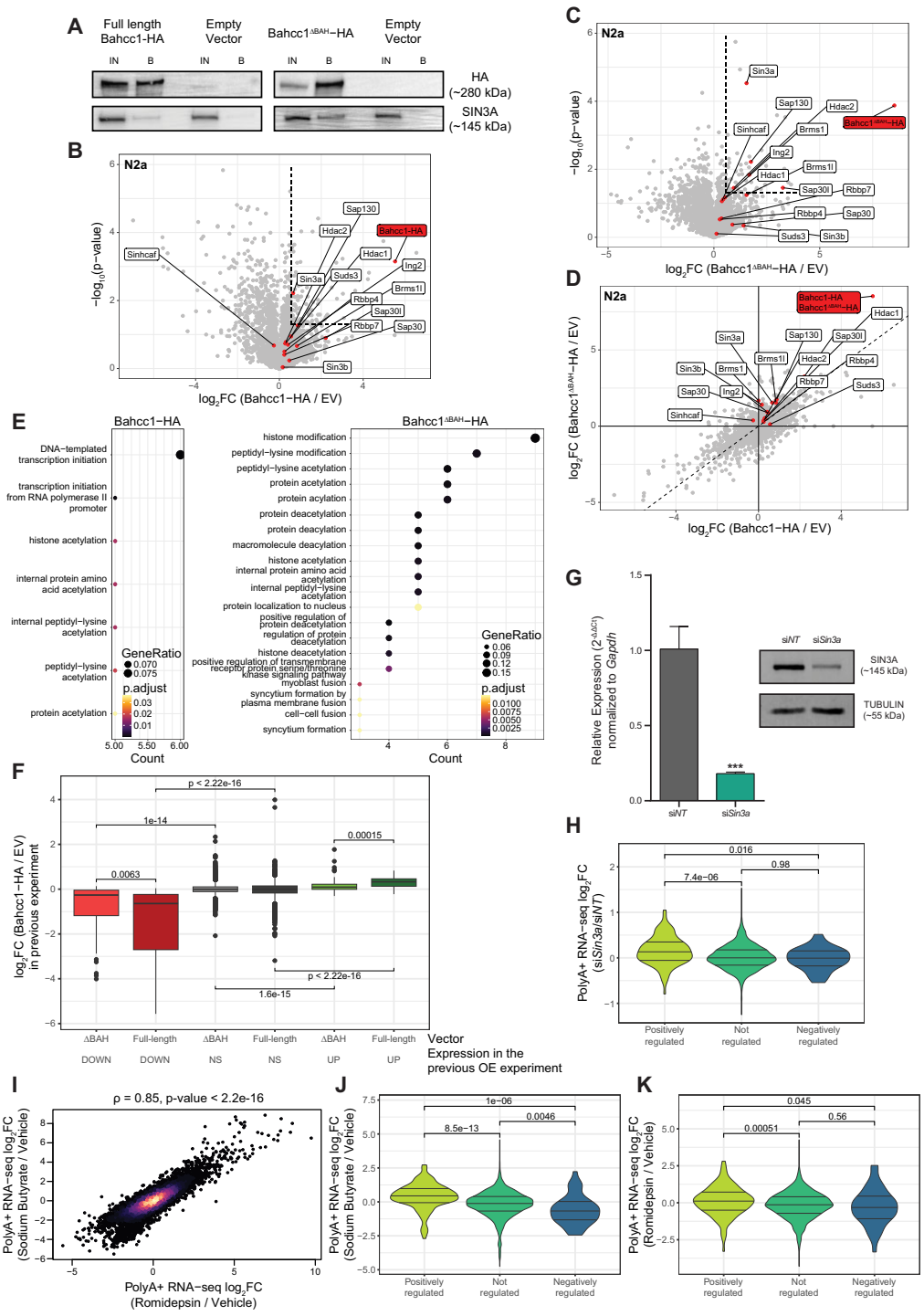

Figure 4. BAHCC1 associates with SIN3A and counteracts SIN3–HDAC activity. (**A**) Co-immunoprecipitation of BAHCC1 and SIN3A in N2a cells (IN = input, B = bound fraction). (**B**) Volcano plot showing the magnitude and significance for the proteins identified by LC-MS after pulling down BAHCC1-HA in N2a cells. The dashed lines represent the *P*-value and $\log_2$FC thresholds, and all the core members of the SIN3A-HDAC complex have been highlighted. (**C**) Same as in panel (B), but after pulling down BAHCC1$^{\Delta BAH}$-HA. (**D**) Correspondence between the enrichments after immunoprecipitation of the full-length BAHCC1 and BAHCC1$^{\Delta BAH}$. The thick lines represent a $\log_2$FC equal to 0, and the dotted line is the identity line. (**E**) GO enrichment of the significantly enriched proteins in the BAHCC1-HA (left) and BAHCC1$^{\Delta BAH}$-HA (right) pulldowns. (**F**) Changes in gene expression of the differentially expressed genes identified in Fig. 2B upon the transfection of a full length *Bahcc1-HA* or *Bahcc1$^{\Delta BAH}$-HA* vector. (**G**) RT-qPCR (left) and western blot (right) upon *Sin3a* depletion with siRNAs to assess KD efficiency. (**H**) Changes in gene expression upon *Sin3a* KD for the positively and negatively regulated genes by BAHCC1. (**I**) Correspondence between changes in gene expression after treatment of N2a cells with sodium butyrate and romidepsin. Color indicates local point density. (**J**) Same as in panel (H), but after treating cells with sodium butyrate (pan-HDAC inhibitor). (**K**) Same as in panel (J), but after treating cells with romidepsin (class I-specific HDAC inhibitor). All experiments were performed in $n = 3$ biological replicates, with the error bars in the barplots representing the standard deviation, *P*-value > .05 = ns; < .05 = *, < .01 = **; < .001 = *** (two-tailed Student's *t*-test). In all violin plots, the three lines represent the median, first and third quartiles, and significance of the different comparisons was calculated by using a Mann–Whitney test. Proteins in the MS experiments were considered to be significantly enriched in the eluates when *P*-value < .05 and FC > 1.5. Genes were considered to be differentially expressed when adj. $P < .05$ and $|\log_2 FC| > .41$ (corresponding to a change of 33%).

responses were highly correlated (Fig. 4I, $R = 0.85, P < 10^{-15}$), and when considering genes regulated by BAHCC1, both HDAC inhibitions upregulated positively regulated genes and downregulated the negatively regulated ones (Fig. 4J and K), supporting the notion that these genes are regulated by BAHCC1 at least in part via histone acetylation.

These results are consistent with a model in which BAHCC1 is generally associated with H3K27ac-decorated regions, where its binding partners within the SIN3A complex are also recruited. At a subset of regions with stronger BAHCC1 association, BAHCC1 is positively regulating H3K27ac levels, possibly by inhibiting the HDAC activity of the SIN3A complex, which preferentially occupies promoter regions, but is also found at the BAHCC1-bound distal sites.

BAHCC1 regulates histone acetylation and gene expression in primary cortical neurons

To test the relevance of the N2a cell line data in primary cells, we used the *Bahcc1*-targeting GapmeRs to knock down *Bahcc1* in cultured primary mouse cortical neurons (Fig. 5A). Gapmer #1 was more effective in this system and thus was used in further experiments (Fig. 5A). We profiled BAHCC1, H3K27ac, H3K27me3, and H3K4me3 chromatin occupancy, changes in gene expression by RNA-seq, and changes in H3K27ac following GapmeRs free uptake. Consistently with the data in N2a cells, BAHCC1 binding was associated with active promoters (Fig. 5B), most correlated with H3K27ac histone mark (Fig. 5C), and knockdown by *Bahcc1* led to a decrease in H3K27ac levels in the peaks most strongly occupied by BAHCC1 (Fig. 5D). When considering changes in gene expression, *Bahcc1* KD led to significant changes in gene expression (Fig. 5E) and the up-regulated genes were enriched for terms related to synaptic and neurotransmitter signaling (Fig. 5F), whereas the down-regulated ones were enriched with genes acting in cell motility and neuronal development (Fig. 5G), consistent with the trends in the N2a data. Indeed, there was a weak yet significant correlation between changes in gene expression upon *Bahcc1* KD in N2a and in the primary cortical neurons ($R = 0.12, P < 10^{-15}$). Among the 26 genes found to be significantly downregulated in both N2a and cortical neurons, some were previously linked to different functions in the nervous system, such as *Tnr* [53], *Gfra1* (GDNF receptor) [54, 55] and *Dkk3* [56]. Of the 13 commonly upregulated genes, *Vgf* has been extensively linked to Alzheimer's Disease (AD) and cognitive functions [57–60], *Atf5* to abnormal cortical development [61], *Emc1* to neurodevelopmental delay and cerebellar degeneration [62–65], and *Asns* to microcephaly and neuronal differentiation [66, 67]. We validated the RNA-seq results in cortical neurons and N2a for selected genes by RT-qPCR (Supplementary Fig. S10A–D), and the enrichment of BAHCC1 in selected promoter regions in N2a by CUT&RUN-qPCR (Supplementary Fig. S10E). We then analyzed different neuronal morphological features in *Bahcc1* KD primary cortical neurons using WIS-Neuromath [28] (Fig. 5H), and found that cells with reduced *Bahcc1* expression exhibit reduced total neurite outgrowth (Fig. 5I, top) and number of processes (Fig. 5I, top-center), which were shorter (Fig. 5I, center-bottom) and with fewer branches (Fig. 5I, bottom), suggesting that BAHCC1 activity is important for the development and branching of neurites.

Taken together, our data highlight a role for BAHCC1 in primary cortical neurons, where it affects the expression of several genes important for neuronal biology. These changes are eventually translated into an impaired growth of neurites, both in terms of length and number of branches, suggesting that BAHCC1 plays an important role in neuronal function.

Discussion

This study is to the best of our knowledge the first to address the roles of the BAHCC1 protein in neuronal lineage cells. As such, we performed most of our experiments in the N2a cell line, which is a model enabling efficient transfection of reagents for both KD and OE of this large gene, and allows obtaining large numbers of cells for various assays. Notably, this model is also associated with several limitations in that it is a tumor cell line derived from a mouse neuroblastoma, and thus has altered cellular processes and signalling pathways compared to normal neurons, may exhibit genomic instability over time, and can undergo a degree of spontaneous differentiation. While we note that some of the results also hold true in primary neuronal cultures, and fit phenotypes observed *in vivo* (see below), future studies in primary systems, which can include manipulation of BAHCC1 in the developing brain by *ex utero* electroporation followed by cell tracking, and isolating of specific perturbed cellular populations, and/or development of conditional knockout animals, will elucidate the full spectrum of BAHCC1 activities in the nervous system.

The Sin3 complex, first discovered in yeast in 1987 [68, 69] is centered around the SIN3A/SIN3B scaffold proteins in vertebrates. It is generally thought to be repressive, as it contains histone deacetylases, traditionally associated with gene silencing, a function well established in yeast [70]. However, genome-wide occupancy studies in mammalian cells have found the Sin3 complex to be associated with many active promoters and enhancers [13–15]. The diversity of complex isoforms and substoichiometric components has been suggested to underpin this apparent discrepancy [14]. BAHCC1 is a strong candidate for a possible modulator of SIN3A activity (Fig. 6A and 6B). BAHCC1 levels are apparently substoichiometric to SIN3A. In HEK293T cells there are an estimated 1.6×10^3 copies of BAHCC1 compared to 1.9×10^5 estimated copies of SIN3A and at least 3×10^4 copies of the other SIN3A core components HDAC1, SAP30, FAM60A, RBBP4, RBBP7, and ING2 (https://opencell.czbiohub.org/) (Fig. 6A). TNRC18, a paralog of BAHCC1 is also typically more abundant than BAHCC1. Similarly, while *Bahcc1* mRNA is expressed in all mouse tissues and developmental stages, its levels are generally modest, with a slight enrichment in the developing brain [21]. Also, the phenotype of loss of BAHCC1 is less dramatic than that of Sin3. *Sin3a*$^{-/-}$ mouse embryos die before day E6.5 [71] and *Rbbp4*$^{-/-}$ die before E7.5 [72], whereas *Bahcc1*$^{-/-}$ embryos die shortly after birth [27]. All these suggest that although BAHCC1 is consistently recovered in pulldowns of Sin3 complex components in various systems (Fig. 4A–C, Supplementary S7A, S7B and [13, 16, 23–26]), it is not a core component of this complex but rather plays an auxiliary, and likely regulatory role. We note that while we observe a correlation between BAHCC1 occupancy and decreased SIN3A activity, a more definitive demonstration for a direct inhibitory activity towards SIN3A/HDAC1 complex will require understanding the nature of the molecular interaction between the proteins involved and establishing methods to directly measure HDAC activity by this complex *in vitro* or *in vivo*.

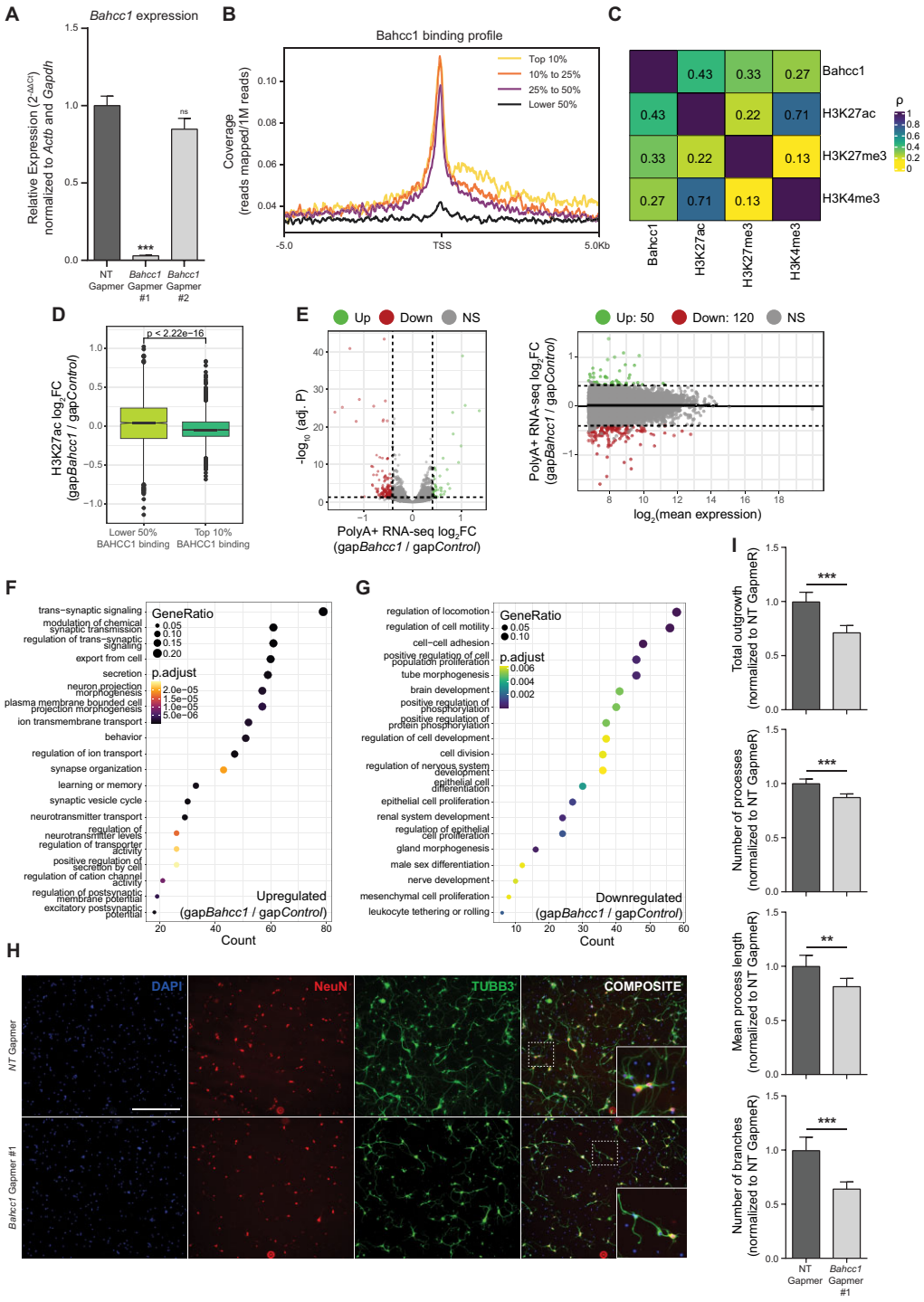

Figure 5. BAHCC1 affects gene expression and neurite outgrowth in primary cortical neurons. (**A**) RT-qPCR after 10 days of gymnotic transfer of *Bahcc1*-targeting GapmeRs in primary cortical neurons to assess KD efficiency. (**B**) Metagene profile around TSS of the normalized BAHCC1 CUT&RUN signal in primary cortical neurons, stratified by gene expression levels. (**C**) Heatmap for the correlations of the CUT&RUN coverage between the examined proteins and histone modifications. Colors and numbers represent the Spearman's correlation coefficients. (**D**) Changes in H3K27ac after *Bahcc1* KD at peaks with the lower 50% and top 10% average coverage of BAHCC1 CUT&RUN reads. (**E**) Volcano (left) and MA (right) plots showing the gene expression changes in primary cortical neurons cultured with *Bahcc1*-targeting GapmeRs. (**F**) GO enrichment analysis of the upregulated genes following *Bahcc1* KD with GapmeRs. (**G**) Same as panel (F), but for the downregulated genes. (**H**) Representative images of primary cortical neurons 10 days after introduction of *Bahcc1*-targeting or control GapmeRs, stained with anti-TUBB3 and anti-NeuN antibodies (scale bar = 200 μm, 10× magnification). (**I**) Normalized neurite outgrowth (top), number of processes (top-middle), average process length (middle-bottom) and number of branches (bottom) in primary cortical neurons cultivated in the presence of either *Bahcc1*-targeting or control GapmeRs. All experiments were performed in $n = 3$ biological replicates, except for neuronal morphological analyses which were done with $n = 6$, with the error bars in the barplots representing the standard deviation. $P > .05$ = ns; $< .05$ = *, $< .01$ = **; $< .001$ = *** (two-tailed Student's *t*-test). For the boxplot in panel (D), the thick line, edges of the box, and whiskers represent the median, first and third quartiles, and the upper and lower 1.5 interquartile ranges (IQRs), respectively. Outliers (observations outside the 1.5 IQRs) are drawn as single points, and the significance was calculated by a two-sided Wilcoxon rank-sum test. Genes were considered to be differentially expressed when adj. $P < .05$ and $|\log_2 FC| > .41$ (corresponding to a change of 33%).

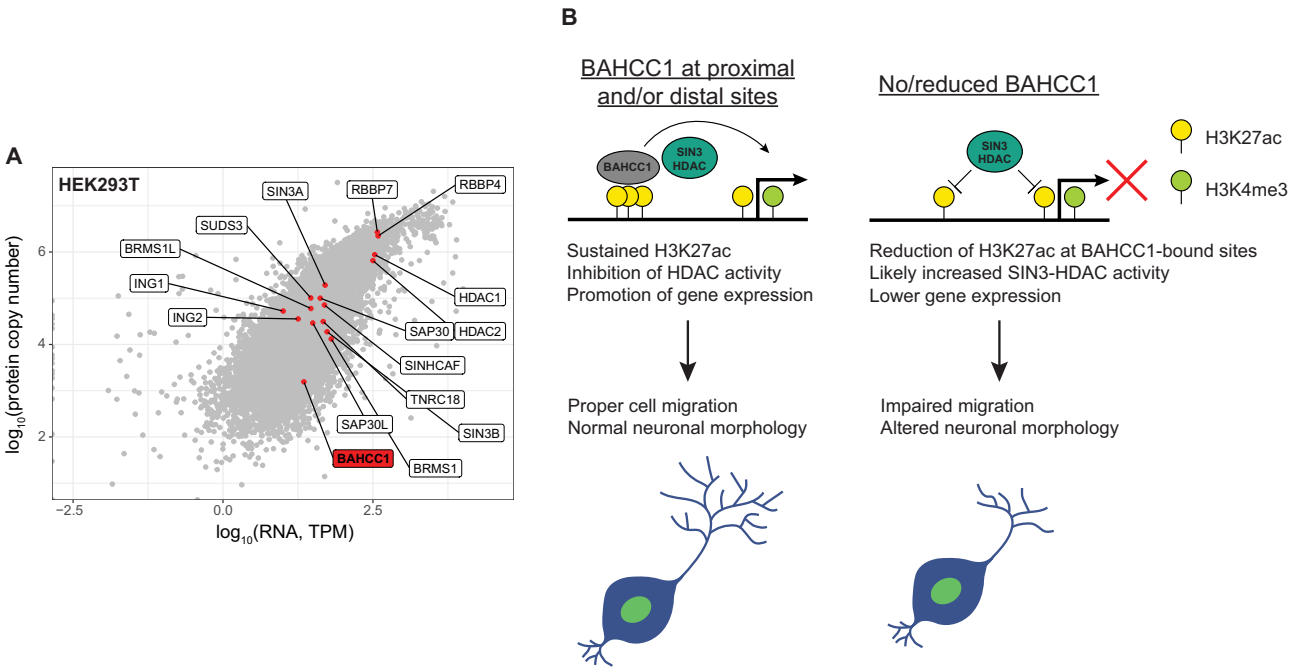

Figure 6. BAHCC1 acts substoichiometrically to modulate SIN3–HDAC. (**A**) RNA and corresponding protein levels for SIN3 components and BAHCC1 in HEK293T cells (data from https://opencell.czbiohub.org/). (**B**) Proposed model for BAHCC1 modulatory activity on SIN3–HDAC.

Interestingly, we find that genes positively regulated by BAHCC1 are up-regulated by KD of *Sin3a*, but also significantly down-regulated by loss of *Sin3b* (Fig. 4H and Supplementary S9D). Consistently, perturbations of SIN3A and SIN3B described in the literature result in different phenotypes [73, 74] and even opposing effects on breast cancer metastasis [75], in line with the differences between their patterns of protein–protein interactions [76]. Still, the relationship between the two proteins and the complexes they scaffold is largely unknown. Intriguingly, we did not find any correlation between the effects of *Sin3a* and *Sin3b* knockdowns ($R = 0.02$; $P = 0.09$), so we suggest that BAHCC1 target sites may define regions with specific opposing effects of the two proteins, which can be further elucidated in future studies. Moreover, BAHCC1 pulldown in N2a (Fig. 4B and 4C) and HEK293T (Supplementary Fig. S7A and S7B) cells specifically retrieved SIN3A but not SIN3B, further suggesting that BAHCC1 function is primarily linked to the former and mostly affects the activity of the SIN3A-containing HDAC complexes. FAM60A is a more recently described component of the SIN3A complex, implicated in its functions in mESCs [5, 13]. Here, we observe no consistent effect on BAHCC1/SIN3A when downregulating *Fam60a*, and it might not be involved in histone acetylation and gene expression regulation in the cell lines we used, as we did not recover FAM60A in BAHCC1 pulldowns in both N2a (Fig. 4B and 4C) and HEK293T (Supplementary Fig. S7A and S7B) cells. We also do not observe a consistent effect when knocking down *Hdac1*, possibly because its loss can be mitigated by other HDACs—particularly HDAC2—as observed in some settings [77–79], which in concert with only a partial KD over a course of three days could explain the absence of any major effect of *Hdac1* KD.

We note that the pulldown of the BAHCC1$^{\Delta BAH}$ in N2a (Fig. 4C) appeared more efficient at retrieving other SIN3–HDAC components compared to that of the full-length protein (Fig. 4B). This could be due to a higher transfection efficiency and increased expression of the truncated protein, a weaker chromatin association resulting from the loss of the BAH domain, or a combination of both factors. Notably, expression and IP of both murine proteins in the HEK293T human cell line specifically recovered almost only SIN3–HDAC factors (Supplementary Fig. S7A and S7B), alluding that these interactions are evolutionarily conserved and functionally more relevant than the others. We additionally demonstrate that the interaction between BAHCC1 and SIN3A is BAH-independent (Fig. 4C and Supplementary S7B), consistent with this domain being primarily involved in engaging H3K27me3 [16]. Nevertheless, BAHCC1$^{\Delta BAH}$ is still functional as the differentially expressed genes following OE of the full length *Bahcc1* are significantly less dysregulated after OE of *Bahcc1*$^{\Delta BAH}$*-HA* (Fig. 4F).

A previous study has linked BAHCC1 primarily to H3K27me3 chromatin marks [16], whereas we do not see any evidence that BAHCC1 co-localizes with H3K27me3 in our CUT&RUN or immunofluorescence data. A possible explanation is that we're generally examining the full-length BAHCC1 protein, whereas [16] mostly studied just its BAH domain that corresponds to < 5% of the full-length protein. Notably, some of our results are consistent with those of [16]. In both studies, KD of HDAC1 and SIN3A components lead to the de-repression of BAHCC1-associated genes. In leukemic cells, the model proposed by Fan et al. was that BAHCC1 recruits SIN3A to regions demarcated by H3K27me3. In our model, BAHCC1-bound regions respond to HDAC inhibition because they are also SIN3A targets, with BAHCC1 likely moderating the efficacy of their repression.

Functionally, we find that loss of BAHCC1 leads to decreased expression of genes enabling cellular migration, and a reduction in N2a motility in transwell migration and wound healing assays, whereas BAHCC1 OE leads to an opposite effect. The ability of neuronal progenitors to migrate is a key

component of their biology [80], and a role for BAHCC1 in enabling this migration may explain its preferential expression in the developing over the adult brain [21]. Consistently with this model, perturbations of BAHCC1 reduced cellular motility and invasiveness in melanoma cells as well [17], and conversely, perturbation of the *SIN3A*, *FAM60A*, and *SUDS3* Sin3 components led to increased invasiveness and enhanced cell migration [25, 75, 81, 82]. In primary mouse cortical neurons harvested from the developing (E16.5/E17) brain, *Bahcc1* depletion caused decreased total neurite outgrowth, with neurons exhibiting fewer and shorter processes, as well as reduced number of branches (Fig. 5I). Future studies will enable testing whether these morphological differences are acompanied with impaired neuronal cell migration *in vivo*, as the two processes are tightly entangled [80]. Defects in cellular morphology following BAHCC1 KD are consistent with the observed transcriptomic changes that mostly encompass genes involved in cell motility, neuronal morphogenesis, synapse development and neurotransmitter signaling. Notably, loss-of-function of some of the BAHCC1-regulated genes are associated with relevant phenotypes, such as GFRα1 [55], Dkk3 [56], Vgf [83], and Atf5 [61].

We previously studied *Bahcc1* in the context of neuronal differentiation of mESCs [21]. In that system genetic manipulation of *Bahcc1* led to massive cell death upon neuronal differentiation, a more drastic phenotype than the one we observe here in more mature cells, possibly because of the only partial knockdown we can achieve with GapmeRs. In our previous study we found that *Bahcc1* perturbation, similarly to the perturbation of the *Reno1* long noncoding RNA, that is transcribed from a region ∼45 Kb upstream of *Bahcc1*, led to a strong differentiation defect, and loss of DNA accessibility at regions marked with H3K4me3. These results are consistent with the model where BAHCC1 affects regions that positively regulate gene expression. We did not examine changes in chromatin marks in that study, and here we find that while there are also changes in H3K4me3 upon BAHCC1 KD (Supplementary Fig. S6D), the more prominent changes are in H3K27ac. Beyond our previous observations, another link between H3K4me3 and BAHCC1 is the large H3K4me3 domain in the gene encoding it [22] that remains to be explored. Regarding *Reno1*, early neuronal differentiation entails a very complex series of chromatin remodeling, likely much more than N2a cells before or after RA-directed differentiation. N2a cells express *Reno1*, but only at very low levels of ∼1 FPKM compared to 3–4 FPKM in the early neurons [21], so our attempts to perturb *Reno1* in this system did not lead to consistent results. Interestingly, over-expression of *Reno1* in this system, which leads to expression of *Reno1* far beyond its physiological levels (Supplementary Fig. S11A), down-regulates the genes positively regulated by Bahcc1 (Supplementary Fig. S11B) and is significantly anti-correlated with BAHCC1 OE in N2a cells ($R=-0.42$, $P < 10^{-15}$, Supplementary Fig. S11C), in an apparent contrast to the co-expression and similar functions of the two genes in mESCs. Future studies of *Reno1* in a system with higher levels, such as the developing brain or early NPCs, may shed further light on its roles.

Transcription is regulated by a complex interplay between a large number of different players that act in part by modifying the chromatin and in part by recruiting or repelling different components of the transcription initiation or elongation/pause-release machinery. This process is likely most complex in the lineages where cell division is limited, and where there is a large diversity of cell types, such as the developing and the mature nervous system. The preferential expression of *Bahcc1* in the brain, and in particular in the developing brain [21], and the neuronal phenotypes in the *Bahcc1*$^{-/-}$ mice suggest that it plays a prominent role in sculpting gene expression in the developing and potentially the mature brain.

Acknowledgements

We thank members of the Ulitsky lab for insightful discussions and comments on the manuscript. We thank Meital Kupervaser (de Botton Institute for Protein Profiling, The Nancy and Stephen Grand Israel National Center for Personalized Medicine, Weizmann Institute of Science) for helping and analyzing the mass spectrometry data. We thank Ida Rishal for technical help with neurite length experiments.

Author contributions: Alan Monziani (Conceptualization [equal], Data curation [lead], Formal analysis [lead], Investigation [lead], Methodology [lead], Software [lead], Validation [lead], Visualization [lead], Writing—original draft [equal], Writing—review & editing [equal]), Rotem Ben-Tov Perry (Formal analysis [supporting], Investigation [supporting], Methodology [supporting]), Hadas Hezroni (Investigation [supporting], Methodology [supporting]), Igor Ulitsky (Conceptualization [equal], Formal analysis [supporting], Funding acquisition [lead], Investigation [supporting], Methodology [supporting], Software [supporting], Supervision [lead], Writing—original draft [equal], Writing—review & editing [equal]).

Supplementary data

Supplementary data is available at NAR online.

Conflict of interest

None declared.

Funding

This work was supported by the ERC Consolidator Grant lncIMPACT to IU and by the Helen and Martin Kimmel Institute for Stem Cell research. Funding to pay the Open Access publication charges for this article was provided by ERC grant.

Data availability

All the RNA-seq and CUT&RUN data are available at the GEO database accession GSE281267. The mass spectrometry data have been deposited in the PRIDE database under the accession PXD058811.

References

1. Nicholson TB, Veland N, Chen T. Chapter 3—writers, readers, and erasers of epigenetic marks. In: Gray SG (ed.), *Epigenetic Cancer Therapy*. Boston: Academic Press, 2015, 31–66.
2. Martire S, Banaszynski LA. The roles of histone variants in fine-tuning chromatin organization and function. *Nat Rev Mol Cell Biol* 2020;**21**:522–41. https://doi.org/10.1038/s41580-020-0262-8

3. Gourisankar S, Krokhotin A, Wenderski W *et al.* Context-specific functions of chromatin remodellers in development and disease. *Nat Rev Genet* 2024;**25**:340–61. https://doi.org/10.1038/s41576-023-00666-x
4. Banks CAS, Zhang Y, Miah S *et al.* Integrative modeling of a Sin3/HDAC complex sub-structure. *Cell Rep* 2020;**31**:107516. https://doi.org/10.1016/j.celrep.2020.03.080
5. Nabeshima R, Nishimura O, Maeda T *et al.* Loss of Fam60a, a Sin3a subunit, results in embryonic lethality and is associated with aberrant methylation at a subset of gene promoters. *eLife* 2018;**7**:e36435. https://doi.org/10.7554/eLife.36435
6. Cowley SM, Iritani BM, Mendrysa SM *et al.* The mSin3A chromatin-modifying complex is essential for embryogenesis and T-cell development. *Mol Cell Biol* 2005;**25**:6990–7004. https://doi.org/10.1128/MCB.25.16.6990-7004.2005
7. Lagger G, O'Carroll D, Rembold M *et al.* Essential function of histone deacetylase 1 in proliferation control and CDK inhibitor repression. *EMBO J* 2002;**21**:2672–81. https://doi.org/10.1093/emboj/21.11.2672
8. David G, Turner GM, Yao Y *et al.* mSin3-associated protein, mSds3, is essential for pericentric heterochromatin formation and chromosome segregation in mammalian cells. *Genes Dev* 2003;**17**:2396–405. https://doi.org/10.1101/gad.1109403
9. Roopra A, Sharling L, Wood IC *et al.* Transcriptional repression by neuron-restrictive silencer factor is mediated via the Sin3-histone deacetylase complex. *Mol Cell Biol* 2000;**20**:2147–57. https://doi.org/10.1128/MCB.20.6.2147-2157.2000
10. Grzenda A, Lomberk G, Zhang J-S *et al.* Sin3: master scaffold and transcriptional corepressor. *Biochim Biophys Acta* 2009;**1789**:443–50. https://doi.org/10.1016/j.bbagrm.2009.05.007
11. Laherty CD, Yang WM, Sun JM *et al.* Histone deacetylases associated with the mSin3 corepressor mediate mad transcriptional repression. *Cell* 1997;**89**:349–56. https://doi.org/10.1016/S0092-8674(00)80215-9
12. Konermann S, Brigham MD, Trevino A *et al.* Optical control of mammalian endogenous transcription and epigenetic states. *Nature* 2013;**500**:472–6. https://doi.org/10.1038/nature12466
13. Streubel G, Fitzpatrick DJ, Oliviero G *et al.* Fam60a defines a variant Sin3a-Hdac complex in embryonic stem cells required for self-renewal. *EMBO J* 2017;**36**:2216–32. https://doi.org/10.15252/embj.201696307
14. van Oevelen C, Wang J, Asp P *et al.* A role for mammalian Sin3 in permanent gene silencing. *Mol Cell* 2008;**32**:359–70. https://doi.org/10.1016/j.molcel.2008.10.015
15. van Oevelen C, Bowman C, Pellegrino J *et al.* The mammalian Sin3 proteins are required for muscle development and sarcomere specification. *Mol Cell Biol* 2010;**30**:5686–97. https://doi.org/10.1128/MCB.00975-10
16. Fan H, Lu J, Guo Y *et al.* BAHCC1 binds H3K27me3 via a conserved BAH module to mediate gene silencing and oncogenesis. *Nat Genet* 2020;**52**:1384–96. https://doi.org/10.1038/s41588-020-00729-3
17. Berico P, Nogaret M, Cigrang M *et al.* Super-enhancer-driven expression of BAHCC1 promotes melanoma cell proliferation and genome stability. *Cell Rep* 2023;**42**:113363. https://doi.org/10.1016/j.celrep.2023.113363
18. Zhao S, Lu J, Pan B *et al.* TNRC18 engages H3K9me3 to mediate silencing of endogenous retrotransposons. *Nature* 2023;**623**:633–42. https://doi.org/10.1038/s41586-023-06688-z
19. Katsuyama T, Sugawara T, Tatsumi M *et al.* Involvement of winged eye encoding a chromatin-associated bromo-adjacent homology domain protein in disc specification. *Proc Natl Acad Sci USA* 2005;**102**:15918–23. https://doi.org/10.1073/pnas.0507945102
20. Masuko K, Fuse N, Komaba K *et al.* winged eye induces transdetermination of *Drosophila* imaginal disc by acting in concert with a histone methyltransferase, su(var)3-9. *Cell Rep* 2018;**22**:206–17. https://doi.org/10.1016/j.celrep.2017.11.105
21. Hezroni H, Ben-Tov Perry R, Gil N *et al.* Regulation of neuronal commitment in mouse embryonic stem cells by the Reno1/Bahcc1 locus. *EMBO Rep* 2020;**21**:e51264. https://doi.org/10.15252/embr.202051264
22. Benayoun BA, Pollina EA, Ucar D *et al.* H3K4me3 Breadth is linked to cell identity and transcriptional consistency. *Cell* 2015;**163**:1281–6. https://doi.org/10.1016/j.cell.2015.10.051
23. McDonel P, Demmers J, Tan DWM *et al.* Sin3a is essential for the genome integrity and viability of pluripotent cells. *Dev Biol* 2012;**363**:62–73. https://doi.org/10.1016/j.ydbio.2011.12.019
24. Banks CAS, Thornton JL, Eubanks CG *et al.* A structured workflow for mapping human Sin3 histone deacetylase complex interactions using halo-MudPIT affinity-purification mass spectrometry. *Mol Cell Proteomics* 2018;**17**:1432–47. https://doi.org/10.1074/mcp.TIR118.000661
25. Smith KT, Sardiu ME, Martin-Brown SA *et al.* Human family with sequence similarity 60 member A (FAM60A) protein: a new subunit of the Sin3 deacetylase complex. *Mol Cell Proteomics* 2012;**11**:1815–28. https://doi.org/10.1074/mcp.M112.020255
26. Huttlin EL, Bruckner RJ, Navarrete-Perea J *et al.* Dual proteome-scale networks reveal cell-specific remodeling of the human interactome. *Cell* 2021;**184**:3022–40. https://doi.org/10.1016/j.cell.2021.04.011
27. Nakayama M, Iida M, Koseki H *et al.* A gene-targeting approach for functional characterization of KIAA genes encoding extremely large proteins. *FASEB J* 2006;**20**:1718–20. https://doi.org/10.1096/fj.06-5952fje
28. Rishal I, Golani O, Rajman M *et al.* WIS-NeuroMath enables versatile high throughput analyses of neuronal processes. *Dev Neurobiol* 2013;**73**:247–56. https://doi.org/10.1002/dneu.22061
29. Algranati D, Oren R, Dassa B *et al.* Dual targeting of histone deacetylases and MYC as potential treatment strategy for H3-K27M pediatric gliomas. *eLife* 2024;**13**:RP96257. https://doi.org/10.7554/eLife.96257.3
30. Elinger D, Gabashvili A, Levin Y. Suspension trapping (S-Trap) is compatible with typical protein extraction buffers and detergents for bottom-up proteomics. *J Proteome Res* 2019;**18**:1441–5. https://doi.org/10.1021/acs.jproteome.8b00891
31. Millikin RJ, Solntsev SK, Shortreed MR *et al.* Ultrafast peptide label-free quantification with FlashLFQ. *J Proteome Res* 2018;**17**:386–91. https://doi.org/10.1021/acs.jproteome.7b00608
32. Miller RM, Millikin RJ, Hoffmann CV *et al.* Improved protein inference from multiple protease bottom-up mass spectrometry data. *J Proteome Res* 2019;**18**:3429–38. https://doi.org/10.1021/acs.jproteome.9b00330
33. Meers MP, Bryson TD, Henikoff JG *et al.* Improved CUT&RUN chromatin profiling tools. *eLife* 2019;**8**:e46314.
34. Martin M. Cutadapt removes adapter sequences from high-throughput sequencing reads. *EMBnet J* 2011;**17**:10. https://doi.org/10.14806/ej.17.1.200
35. Dobin A, Davis CA, Schlesinger F *et al.* STAR: ultrafast universal RNA-seq aligner. *Bioinformatics* 2013;**29**:15–21. https://doi.org/10.1093/bioinformatics/bts635
36. Love M, Anders S, Huber W. Differential analysis of count data–the DESeq2 package. *Genome Biol* 2014;**15**:550. https://doi.org/10.1186/s13059-014-0550-8
37. Wu T, Hu E, Xu S *et al.* clusterProfiler 4.0: a universal enrichment tool for interpreting omics data. *Innovation (Camb)* 2021;**2**:100141.
38. Langmead B, Salzberg SL. Fast gapped-read alignment with Bowtie 2. *Nat Methods* 2012;**9**:357–9. https://doi.org/10.1038/nmeth.1923
39. Zhang Y, Liu T, Meyer CA *et al.* Model-based analysis of ChIP-seq (MACS). *Genome Biol* 2008;**9**:R137. https://doi.org/10.1186/gb-2008-9-9-r137
40. Stovner EB, Sætrom P. epic2 efficiently finds diffuse domains in ChIP-seq data. *Bioinformatics* 2019;**35**:4392–3. https://doi.org/10.1093/bioinformatics/btz232

41. Heinz S, Benner C, Spann N *et al.* Simple combinations of lineage-determining transcription factors prime cis-regulatory elements required for macrophage and B cell identities. *Mol Cell* 2010;**38**:576–89. https://doi.org/10.1016/j.molcel.2010.05.004
42. Quinlan AR, Hall IM. BEDTools: a flexible suite of utilities for comparing genomic features. *Bioinformatics* 2010;**26**:841–2. https://doi.org/10.1093/bioinformatics/btq033
43. Ramírez F, Ryan DP, Grüning B *et al.* deepTools2: a next generation web server for deep-sequencing data analysis. *Nucleic Acids Res* 2016;**44**:W160–5. https://doi.org/10.1093/nar/gkw257
44. Suarez-Arnedo A, Torres Figueroa F, Clavijo C *et al.* An image J plugin for the high throughput image analysis of *in vitro* scratch wound healing assays. *PLoS One* 2020;**15**:e0232565. https://doi.org/10.1371/journal.pone.0232565
45. Lim KRQ, Yokota T. Invention and early history of gapmers. *Methods Mol Biol* 2020;**2176**:3–19.
46. Marzinke MA, Clagett-Dame M. The all-trans retinoic acid (atRA)-regulated gene Calmin (Clmn) regulates cell cycle exit and neurite outgrowth in murine neuroblastoma (Neuro2a) cells. *Exp Cell Res* 2012;**318**:85–93. https://doi.org/10.1016/j.yexcr.2011.10.002
47. Tremblay RG, Sikorska M, Sandhu JK *et al.* Differentiation of mouse Neuro 2A cells into dopamine neurons. *J Neurosci Methods* 2010;**186**:60–7. https://doi.org/10.1016/j.jneumeth.2009.11.004
48. Goswami P, Banks CAS, Thornton J *et al.* Distinct regions within SAP25 recruit O-linked glycosylation, DNA demethylation, and ubiquitin ligase and hydrolase activities to the Sin3/HDAC complex. *J Proteome Res* 2024;**23**:5016–29. https://doi.org/10.1021/acs.jproteome.4c00498
49. Yang X, Zhang F, Kudlow JE. Recruitment of O-GlcNAc transferase to promoters by corepressor mSin3A: coupling protein O-GlcNAcylation to transcriptional repression. *Cell* 2002;**110**:69–80. https://doi.org/10.1016/S0092-8674(02)00810-3
50. Chen M, Chen X, Li S *et al.* An epigenetic mechanism underlying chromosome 17p deletion-driven tumorigenesis. *Cancer Discov* 2021;**11**:194–207. https://doi.org/10.1158/2159-8290.CD-20-0336
51. Singh RN, Howell MD, Ottesen EW *et al.* Diverse role of survival motor neuron protein. *Biochim Biophys Acta Gene Regul Mech* 2017;**1860**:299–315. https://doi.org/10.1016/j.bbagrm.2016.12.008
52. VanderMolen KM, McCulloch W, Pearce CJ *et al.* Romidepsin (Istodax, NSC 630176, FR901228, FK228, depsipeptide): a natural product recently approved for cutaneous T-cell lymphoma. *J Antibiot* 2011;**64**:525–31. https://doi.org/10.1038/ja.2011.35
53. Wagner M, Lévy J, Jung-Klawitter S *et al.* Loss of TNR causes a nonprogressive neurodevelopmental disorder with spasticity and transient opisthotonus. *Genet Med* 2020;**22**:1061–8. https://doi.org/10.1038/s41436-020-0768-7
54. Cacalano G, Fariñas I, Wang LC *et al.* GFRalpha1 is an essential receptor component for GDNF in the developing nervous system and kidney. *Neuron* 1998;**21**:53–62. https://doi.org/10.1016/S0896-6273(00)80514-0
55. Bonafina A, Trinchero MF, Ríos AS *et al.* GDNF and GFRα1 are required for proper integration of adult-born hippocampal neurons. *Cell Rep* 2019;**29**:4308–19. https://doi.org/10.1016/j.celrep.2019.11.100
56. Martin Flores N, Podpolny M, McLeod F *et al.* Downregulation of Dickkopf-3, a Wnt antagonist elevated in Alzheimer's disease, restores synapse integrity and memory in a disease mouse model. *eLife* 2024;**12**:RP89453. https://doi.org/10.7554/eLife.89453.3
57. Beckmann ND, Lin W.-J, Wang M *et al.* Multiscale causal networks identify VGF as a key regulator of Alzheimer's disease. *Nat Commun* 2020;**11**:3942. https://doi.org/10.1038/s41467-020-17405-z
58. El Gaamouch F, Audrain M, Lin W.-J *et al.* VGF-derived peptide TLQP-21 modulates microglial function through C3aR1 signaling pathways and reduces neuropathology in 5xFAD mice. *Mol Neurodegener* 2020;**15**:4. https://doi.org/10.1186/s13024-020-0357-x
59. Mizoguchi T, Minakuchi H, Ishisaka M *et al.* Behavioral abnormalities with disruption of brain structure in mice overexpressing VGF. *Sci Rep* 2017;**7**:4691. https://doi.org/10.1038/s41598-017-04132-7
60. Yu L, Petyuk VA, Lopes K *et al.* Associations of VGF with neuropathologies and cognitive health in older adults. *Ann Neurol* 2023;**94**:232–44. https://doi.org/10.1002/ana.26676
61. Umemura M, Kaneko Y, Tanabe R *et al.* ATF5 deficiency causes abnormal cortical development. *Sci Rep* 2021;**11**:7295. https://doi.org/10.1038/s41598-021-86442-5
62. Chung H.-L, Rump P, Lu D *et al.* *De novo* variants in EMC1 lead to neurodevelopmental delay and cerebellar degeneration and affect glial function in *Drosophila*. *Hum Mol Genet* 2022;**31**:3231–44. https://doi.org/10.1093/hmg/ddac053
63. Cabet S, Lesca G, Labalme A *et al.* Novel truncating and missense variants extending the spectrum of EMC1-related phenotypes, causing autism spectrum disorder, severe global development delay and visual impairment. *Eur J Med Genet* 2020;**63**:103897. https://doi.org/10.1016/j.ejmg.2020.103897
64. Geetha TS, Lingappa L, Jain AR *et al.* A novel splice variant in EMC1 is associated with cerebellar atrophy, visual impairment, psychomotor retardation with epilepsy. *Mol Genet Genomic Med* 2018;**6**:282–7. https://doi.org/10.1002/mgg3.352
65. Harel T, Yesil G, Bayram Y *et al.* Monoallelic and biallelic variants in EMC1 identified in individuals with global developmental delay, hypotonia, scoliosis, and cerebellar atrophy. *Am J Hum Genet* 2016;**98**:562–70. https://doi.org/10.1016/j.ajhg.2016.01.011
66. Schleinitz D, Seidel A, Stassart R *et al.* Novel mutations in the asparagine synthetase gene (ASNS) associated with microcephaly. *Front Genet* 2018;**9**:245. https://doi.org/10.3389/fgene.2018.00245
67. Appiah B, Fullio CL, Ossola C *et al.* DOT1L activity affects neural stem cell division mode and reduces differentiation and ASNS expression. *EMBO Rep* 2023;**24**:e56233. https://doi.org/10.15252/embr.202256233
68. Nasmyth K, Stillman D, Kipling D. Both positive and negative regulators of HO transcription are required for mother-cell-specific mating-type switching in yeast. *Cell* 1987;**48**:579–87. https://doi.org/10.1016/0092-8674(87)90236-4
69. Sternberg PW, Stern MJ, Clark I *et al.* Activation of the yeast HO gene by release from multiple negative controls. *Cell* 1987;**48**:567–77. https://doi.org/10.1016/0092-8674(87)90235-2
70. Kadamb R, Mittal S, Bansal N *et al.* Sin3: insight into its transcription regulatory functions. *Eur J Cell Biol* 2013;**92**:237–46. https://doi.org/10.1016/j.ejcb.2013.09.001
71. Dannenberg J.-H, David G, Zhong S *et al.* mSin3A corepressor regulates diverse transcriptional networks governing normal and neoplastic growth and survival. *Genes Dev* 2005;**19**:1581–95. https://doi.org/10.1101/gad.1286905
72. Miao X, Sun T, Barletta H *et al.* Loss of RBBP4 results in defective inner cell mass, severe apoptosis, hyperacetylated histones and preimplantation lethality in mice†. *Biol Reprod* 2020;**103**:13–23. https://doi.org/10.1093/biolre/ioaa046
73. David G, Grandinetti KB, Finnerty PM *et al.* Specific requirement of the chromatin modifier mSin3B in cell cycle exit and cellular differentiation. *Proc Natl Acad Sci USA* 2008;**105**:4168–72. https://doi.org/10.1073/pnas.0710285105
74. Heideman MR, Lancini C, Proost N *et al.* Sin3a-associated Hdac1 and Hdac2 are essential for hematopoietic stem cell homeostasis and contribute differentially to hematopoiesis. *Haematologica* 2014;**99**:1292–303. https://doi.org/10.3324/haematol.2013.092643
75. Lewis MJ, Liu J, Libby EF *et al.* SIN3A and SIN3B differentially regulate breast cancer metastasis. *Oncotarget* 2016;**7**:78713–25. https://doi.org/10.18632/oncotarget.12805
76. Adams MK, Banks CAS, Thornton JL *et al.* Differential complex formation via paralogs in the Human Sin3 protein interaction

Network. *Mol Cell Proteomics* 2020;**19**:1468–84. https://doi.org/10.1074/mcp.RA120.002078
77. Zhao P, Wang H, Wang H *et al.* Essential roles of HDAC1 and 2 in lineage development and genome-wide DNA methylation during mouse preimplantation development. *Epigenetics* 2020;**15**:369–85. https://doi.org/10.1080/15592294.2019.1669375
78. Zhao P, Li S, Wang H *et al.* Sin3a regulates the developmental progression through morula-to-blastocyst transition Hdac1. *FASEB J* 2019;**33**:12541–53. https://doi.org/10.1096/fj.201901213R
79. Montgomery RL, Davis CA, Potthoff MJ *et al.* Histone deacetylases 1 and 2 redundantly regulate cardiac morphogenesis, growth, and contractility. *Genes Dev* 2007;**21**:1790–802. https://doi.org/10.1101/gad.1563807
80. Valiente M, Marín O. Neuronal migration mechanisms in development and disease. *Curr Opin Neurobiol* 2010;**20**:68–78. https://doi.org/10.1016/j.conb.2009.12.003
81. Das TK, Sangodkar J, Negre N *et al.* Sin3a acts through a multi-gene module to regulate invasion in *Drosophila* and human tumors. *Oncogene* 2013;**32**:3184–97. https://doi.org/10.1038/onc.2012.326
82. Davenport ML, Davis MR, Davenport BN *et al.* Suppression of SIN3A by miR-183 promotes breast cancer metastasis. *Mol Cancer Res* 2022;**20**:883–94. https://doi.org/10.1158/1541-7786.MCR-21-0508
83. Sato H, Fukutani Y, Yamamoto Y *et al.* Thalamus-derived molecules promote survival and dendritic growth of developing cortical neurons. *J Neurosci* 2012;**32**:15388–402. https://doi.org/10.1523/JNEUROSCI.0293-12.2012

Received: December 12, 2024. **Revised:** June 12, 2025. **Editorial Decision:** June 13, 2025. **Accepted:** June 20, 2025